



Modeling of unsteady and steady fluid flow, heat transfer and dispersion in porous media using unit cell scale

A.A. Alshare*, P.J. Strykowski, T.W. Simon

Department of Mechanical Engineering, University of Minnesota, 111 Church Street S.E., Minneapolis, MN 55455, USA

ARTICLE INFO

Article history:
Available online 18 January 2010

Keywords:
Porous media
Heat transfer
Unit cell
Heat exchanger
Steady and transient

ABSTRACT

A unit cell scale computation of laminar steady and unsteady fluid flow and heat transfer is presented for a spatially periodic array of square rods representing two-dimensional isotropic or anisotropic porous media. In the model, a unit cell is taken as a representative elementary control volume and uniform heat flux boundary conditions are imposed on the solid–fluid interface. The governing equations are discretized by means of the finite volume approach; boundaries between adjacent cells are taken to be spatially periodic. Computations obtained using the SIMPLER algorithm, are made by varying the macroscopic flow direction from 0° to 90° relative to the unit cell, and varying the Reynolds number over the range 1–10³ spanning the Darcian and the inertial flow regimes to construct a database of local flow and heat transfer resistances in terms of permeabilities, inertial coefficients, Nusselt numbers, and thermal dispersion coefficients. The resulting database is utilized in a system scale analysis of a serpentine heat exchanger, where these directional terms from the microscale analysis provide closure to the porous-continuum model.

© 2009 Elsevier Ltd. All rights reserved.

1. Introduction

There continues to be considerable interest in fluid flow and heat transfer in porous media. This is related to the number of engineering systems having some sort of porous structure through which a working fluid permeates. Non-Darcian flow in porous media and, in particular, fibrous porous media, plays a critical role in many engineered and natural processes. Engineered examples include packed bed reactors, cooling towers, low Reynolds number heat exchangers shell sides, electronic components and filtration devices, as discussed by Shapiro and Brenner [1]; Natural examples relevant to cell mechanics are discussed by Curry and Michel [2]. Porous media in the form of structured arrays have been used to investigate the momentum and energy transport at the unit cell scale or microscale in order to extract system scale or macro-scale parameters.

Larson et al. [3] obtained expressions of the principal permeabilities in terms of solid volume concentration by solving the Stokes flow in square and hexagonal arrays of circular and elliptic cylinders having a porosity in the range of (0.3 ≤ ε ≤ 0.9). Coulaud et al. [4] investigated inertial flows in monodispersed and bidispersed staggered arrays of cylinders in the range of porosity (0.43 ≤ ε ≤ 0.80), and Reynolds number ($Re_d \leq 25$). They showed that dimensionless pressure gradient decreases with increasing

porosity and increases with increasing Reynolds number. Edwards et al. [5] determined the apparent permeability in monodispersed and polydispersed square and hexagonal arrays of cylinders over the porosity range (0.4 ≤ ε ≤ 0.7) and Reynolds number range ($Re_d \leq 200$). They showed that the apparent permeability, which is defined as the ratio of Darcian velocity to the mean pressure gradient, depends upon both the magnitude and direction of the applied pressure gradient and diminishes with increasing solid concentrations and increasing Reynolds numbers. Gahddar et al. [6] determined the permeability of fibrous media made of square and hexagonal monodispersed arrays of circular cylinders in the moderate porosity range (0.40 ≤ ε ≤ 0.80) and Reynolds number range ($Re_d \leq 200$). They found that the creeping unidirectional cross-flow permeability exhibited exponential decay with increasing solid concentration. In contrast, the inertial flow permeability decayed exponentially with increasing Reynolds number for the whole range of solid concentrations. Nagelhout et al. [7] also found that for a square monodispersed arrays in the high porosity range (0.80 ≤ ε ≤ 0.94) and Reynolds number range ($Re_d \leq 40$) that the permeability exponentially decays with both increasing solid concentration and increasing Reynolds number. Martin et al. [8] investigated flow and heat transfer in sparse square and triangular arrays in the high porosity range, (0.80 ≤ ε ≤ 0.99) and Reynolds number range ($Re_d \leq 160$). They illustrated that the friction factor followed a power-law dependency on the Reynolds number. Lee and Yang [9] determined the flow resistance for a bank of cylinders in triangular arrangement in a porosity range (0.43 ≤ ε ≤ 0.94) and Reynolds number range ($Re_d \leq 50$). They found that viscous

* Corresponding author.
E-mail addresses: aalshare@me.umn.edu (A.A. Alshare), pstry@me.umn.edu (P.J. Strykowski), tsimon@me.umn.edu (T.W. Simon).

the Forchheimer tensors and found that the pressure gradient substantially increases with increasing Reynolds number for the case of off-axis flows. Though the three-dimensional extension by these authors [39] is a valuable extension, it is the two-dimensional study [40] that is most germane to the present paper.

Thermal dispersion in porous media is the result of the presence of both microscale temperature and velocity gradients and the application of volume averaging. Dispersion in porous media is analogous to thermal eddy diffusivity in turbulence and is a direct result of the transport occurring at length scales smaller than the REV. Dispersion anisotropy is due to its dependence on the flow direction and the structural anisotropy of the media. Dispersion in periodic structure was formulated by Brenner [14] applying the method of moments. He obtained the dispersion tensor from the moments of the probability density of a particle position by extending Brownian theory for the particle in a periodic unit cell.

Carbonell and Whitaker [15] used the local volume averaging technique to derive the macroscopic energy equation for a unit cell of a porous medium. In their approach, they introduced a vector function \mathbf{b} (transformation), which projects the gradient of averaged volume temperature onto the scalar function of local temperature deviation, such as

$$T' = \mathbf{b} \nabla \langle T \rangle \quad (1)$$

The transformation function is a function of position within the unit cell and is influenced by the hydrodynamics (e.g. Re and structure) thermophysical properties (e.g. Pr and k_s/k_f), and the cell geometry (e.g. structure and ϵ).

Eidsath et al. [16] used the LVAT to evaluate the dispersion tensor for a periodic structure of cylinders and found that at high Péclet numbers the longitudinal dispersion followed the relation $Pe^{1.7}$. Their results for the stream-wise dispersion were in agreement with experimental results of Gunn and Pryce [17]. However, their model predicted a nearly constant lateral dispersion coefficient. It must be noted that in their model, the thermal conductivity is assumed to be zero.

Koch et al. [18] also used LVAT for Stokes flow through an array of spheres and cylinders in the porosity range of ($0.80 \leq \epsilon \leq 0.98$) and obtain closed-form solutions for the dispersion tensor. In their model, the solid phase was assumed to have the same thermal conductivity as the fluid. Their prediction of the stream-wise dispersion coefficient gives a Pe^2 relationship. Edwards et al. [19] examined the effects of porosity, particle arrangement, Prandtl number, and Reynolds number on the dispersion tensor. They found that longitudinal dispersion generally increases with Péclet number at a rate of less than Pe^2 . With increasing Péclet number, however, Pe^2 dependence is approached asymptotically. In this model, the thermal conductivity of the particles is assumed to be zero and no coupling of the energy equations for the fluid and solid phases was present. Sahraoui and Kaviany [20–22] utilized structured arrays of cylinders with a porosity range of ($0.50 \leq \epsilon \leq 0.95$) to determine the longitudinal and lateral dispersion. They investigated the effects of fluid to solid conductivity ratio, Péclet number, array arrangement, and mean flow angle on the dispersion coefficients. They found that longitudinal dispersion have nearly a Pe^2 dependency for the in-line arrangement and approaches Pe for the staggered arrangement. An increase in the flow tilt angle increases the lateral dispersion and decreases the longitudinal dispersion. As the flow tilt angle changes, the exponent of the Pe dependency varies between 0.97 and 1.7.

Arquis et al. [23,24] used in-line and staggered arrays of cylinders to investigate the dispersion coefficients. They obtained the longitudinal and lateral dispersion by posing a macroscopic temperature gradient parallel and perpendicular to the flow direction, respectively. Kuwahara et al. [25,26] applied the method of Arquis to determine the dispersion coefficients using an in-line arrange-

ment of square cylinders. They proposed correlations for the longitudinal and lateral dispersion with Pe^2 and $Pe^{1.7}$ dependency, respectively, for low Péclet numbers. Both dispersion coefficients approached Pe dependency for higher Péclet number. The lateral dispersion was found to be much smaller than the longitudinal dispersion for a range of Péclet numbers. Souto and Moyne [27] also determined the dispersion coefficients for a porous medium of square cylinders. They investigated the influence of order, spatial periodicity, and mean flow direction on the dispersion tensor in both Stokes and inertial flows. They showed that in case of in-line and staggered arrangements, the longitudinal dispersion was found to have a Pe^2 dependency. However, for other flow angles the exponent of Pe^m , m , deviated from 2 and varied widely and can be characterized by an average exponent, $\bar{m} \approx 1.2$. However, for the case of disordered media, the influence of flow angle is weak and for all the cases considered, the average exponent, \bar{m} , was ≈ 1.6 . They showed that the lateral dispersions exhibited rather small values in comparison with the longitudinal dispersion; in the in-line cylinders case, it tends asymptotically toward a constant at high Péclet numbers and for the staggered cylinders, the behavior is shown to depend sharply on the value of the flow angle. For the disordered medium, on the average, the exponent characterizing the lateral coefficient, \bar{m} , is ≈ 0.4 . Didierjean et al. [28] experimentally determined the dispersion tensor for ordered and disordered media consisting of cylinders. Two flow directions (0° and 26°) of the mean velocity vector were investigated in the ordered medium in-line cylinders arrangement. It was found that the exponent of Pe^m for the longitudinal dispersion lies in the range $1.67 \leq m \leq 1.83$, which is much different than the value for Taylor dispersion through a tube. When the flow is posed at 26° to the array, the values of m lie in the range of $1.2 \leq m \leq 1.4$, affirming that the dispersion is significantly influenced by the direction of the mean velocity vector.

The empirical correlation established by Wakao et al. [29] for the interfacial heat transfer of gas flow in porous media continues to be used widely. Wakao et al. collected and scrutinized reliable experimental data published in the literature over the span of four decades on interfacial heat transfer. The correlated data included both steady and unsteady heat transfer experiments in the Reynolds number range of 15–8500. The porous media geometries included spheres, cylinders, and cubes made of various materials. Wakao's correlation for dimensionless heat transfer coefficients in packed beds is based on a form suggested by Ranz et al. [30,31] as $Nu = 2.0 + aRe^m Pr^{1/3}$. The Nusselt number is assumed to approach the limiting value of 2.0 as the Reynolds number is decrease to zero. This applies to a single, isolated sphere in a stagnant fluid. Ranz et al. suggested that $a = 0.6$ and $m = 0.5$. In their review of mass transfer in packed beds, Wako and Kagui [32] found that $a = 1.1$ and $m = 0.6$ would be more consistent with available data. The theoretical value of 2.0 for the Nusselt number for an isolated single sphere has no physical meaning in very low Reynolds number flow through packed beds of particles this is because, at zero Reynolds number, the boundary conditions in a packed bed are quite different from those for an isolated particle [33]. Heat Transfer data were reported by Kays and London [34] for cross-rod, screen, and sphere matrices. The porosities were in the range of ($0.60 \leq \epsilon \leq 0.83$), and the heat transfer coefficient data were correlated in terms of Colburn j -factor with the hydraulic diameter being used in the Reynolds number as the characteristic length. The reported data were only for flows of gas and only within a moderate range of Reynolds numbers. Zukauskas [35] compiled extensive experimental data of heat transfer and hydrodynamic drag of single tube, banks of tubes, and systems of tubes in cross-flow. They considered investigations of tube banks of various arrangements in the range of Prandtl numbers from 0.7 to 500 and Reynolds numbers from 1×10^6 to 2×10^6 . It is asserted that the

heat transfer coefficient in tube banks is dependent on the flow velocity, physical properties of the fluid, heat flux density, and flow direction, as well as the arrangement of the tubes. At low Reynolds numbers ($Re_d \leq 10^3$), the flow in a bank may be described as predominantly laminar, with large-scale vortices in the circulation regions. For the generalization of experimental data, the following power correlation is proposed $Nu = aRe^m Pr^n$. Where, a , m , and n are found to be dependent on tube arrangements and the range of Reynolds number. Kar and Dybbs [36] correlated experimental heat transfer coefficient data in terms of Nusselt number and used the mean pore diameter as the characteristic length in both the Nusselt number and Reynolds number. They gave the following correlation $Nu = aRe^m Pr^{1/3}$, $a = 0.004$, and $m = 1.35$. Also Dybbs and Ling [37] utilized the capillary tube model of porous media such that the REV of the media is a single tube. The REV length scale is considered as the microscopic characteristic length of the porous media in the bulk flow direction. While the average pore diameter is a characteristic length in the plane orthogonal to the flow direction. They proposed introducing the REV length scale, l_{REV} , and the pore scale length, d , into the Nusselt correlation, which is given as $Nu = aRe^m Pr^{1/3} (d/l_{REV})$. They also offered two Nu vs. Re correlations, corresponding to the Darcy and inertial flow regimes. The powers of the Reynolds number in the two regimes are $m \approx 1$ and $m = 1.4$, respectively. Martin et al. [8] determined the Nusselt number for gas flow (air, $Pr \sim 0.7$) in sparse square and triangular arrays of cylinders for the thermal conditions of uniform tube wall temperature and uniform heat flux. They showed that the Nusselt number is directly proportional to the Reynolds number and solid concentration (inverse porosity). The Nusselt number for the uniform heat flux case was found approximately 20% higher than for the uniform tube wall temperature case. They fitted the numerical results into a power-law correlations in the form $Nu = aRe^b$ in which the constants varied in the range $1.1 < a < 2.5$, and $0.14 < b < 0.29$ depending on the porosity and thermal boundary conditions. Kuwahara et al. [38] computed the interfacial heat transfer for a packed bed using a staggered array of square cylinders. The numerical results are fitted using the correlation form suggested by Wakao and Kaguei, $Nu = a + bRe^0.6 Pr^{1/3}$. The coefficients a and b were obtained for range of porosities ($0.2 < \epsilon < 0.9$) and were given as $a = (1 + 4(1 - \epsilon)/\epsilon)$ and $b = 1/2(1 - \epsilon)^{1/2}$. The computed results are found to be in agreement with the experimentally fitted results of Wakao and Kaguei. Nakayama et al. [40] determined the interfacial heat transfer coefficient for gas flow ($Pr \sim 1.0$) in in-line arrays of square cylinders for the thermal condition of uniform wall temperature. The numerical results are correlated using $Nu = c_f + d_f Re_d^0.6 Pr_d^{1/3}$ where the constants c_f and d_f are dependent on the flow angle and porosity. It is noteworthy to mention that Viskanta [41] made a comparison of a few selected heat transfer correlations for convective transport in porous media. They included a single sphere, packed beds formed from spherical particles, and consolidated porous media. The comparisons revealed that there was a large discrepancy between the results, particularly for the low Reynolds number range and that the technical issue of an appropriate length scale for correlating heat transfer data in porous media was not resolved and there was a need for fundamental research attention.

In this work, an array of in-line square cylinders in the porosity range ($0.75 < \epsilon < 0.875$) the Reynolds number range 1.0 – 10^3 is used is utilized to determine the flow resistance and heat transfer resistances offered by an array of square tubes with inline arrangement. The permeability which is a material property could be found by conducting low Reynolds number simulations where as the Forchheimer coefficient is found by carrying out a number of high Reynolds number simulations. The stream-wise and cross-stream thermal dispersion coefficients are found by assuming local thermal equilibrium and imposing a macroscopic temperature gra-

dent, on the unit cell, that is parallel and perpendicular to the mean flow, respectively. The interfacial heat transfer coefficient is obtained from temperature field computation and by imposing uniform heat flux at the solid–fluid interface. The obtained effective properties of the porous media is a preliminary but essential step in the analysis of the porous media.

2. Unit cell model

The main idea here is to use the microscopic details of the geometry of the rod arrangement and flow angularity to determine the effective anisotropic properties of the porous medium. Due to the spatial periodicity of the medium, a unit cell can be analyzed by imposing a varying mean flow direction relative to the unit cell, and a varying Reynolds number. The velocity and temperature fields throughout the domain defined by the unit cell are calculated, which allows us to characterize the porous media in terms of the effective properties. The outcome of the micro-calculations is a database of permeabilities, Forchheimer coefficients, heat transfer coefficients, and thermal dispersion coefficients. Having such a data base provides closure of the porous-continuum model or system scale problem. The sections below give details of unit cell model (micromodel) formulation, the numerical procedure, followed by results and discussion.

2.1. Governing equations

The proposed geometry of a structured porous medium is an infinite number of square rods arranged in a spatially periodic, two-dimensional pattern, as shown schematically in Fig. 1. The unit cell scale (microscale) model is used herein to analyze numerically the details of fluid flow and heat transfer by solving the laminar Navier–Stokes equation on the pore scale. The steady flow is assumed to be laminar and the fluid properties are uniform (unsteady flow calculations on the unit cell is given at the last section of this paper). The spatial variations of the velocity and tempera-

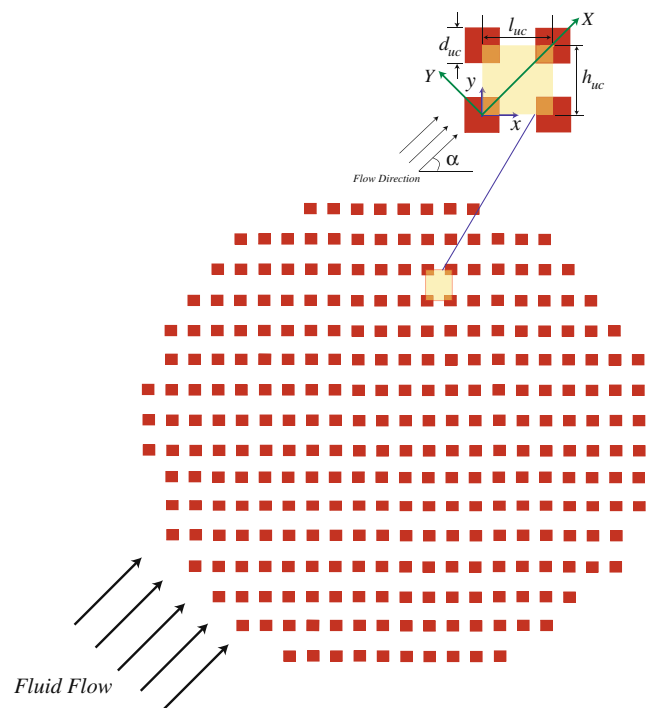


Fig. 1. A structured array of elements representing a model porous medium and a unit cell or representative elementary volume.

ture fields are resolved within a single unit cell, which is considered to be the Representative Elementary Volume (REV). Flow in a structured array attains a periodic, fully-developed behavior after a short entrance region. Patankar et al. [42] formulated the numerical procedure for on-axis, periodically-fully-developed flow. Here, we outline the numerical procedure utilized in the solution of angled, fully-developed flow and the computation of a temperature field for the uniform flux thermal boundary condition.

Consider the flow entering a porous medium, Fig. 1, of a two-dimensional, structured array of uniform-heat-generating, rectangular rods. The macroscopic flow in such a structured array attains a periodic, fully-developed behavior after a short entrance region. The orthotropic structure may be considered to be an anisotropic, porous medium, where the three principal axes of structural symmetry are mutually orthogonal. Because the geometry is spatially periodic for a fully-developed flow, the calculations are confined to the typical cell indicated by the dashed line in Fig. 1. The pressure, p , in periodic, fully-developed flow can be expressed as follows:

$$p(x, y) = -\beta x - \zeta y + P(x, y) \quad (2)$$

Note that the pressure field is decomposed into two parts that vary linearly with the respective coordinate directions at a rate of β and ζ , and a portion that behaves in a periodic fashion from one unit cell to another. The term $\beta x + \zeta y$ is indicative of the global pressure drop that takes place across the unit cell, where $\arctan(\zeta/\beta)$ determines the orientation of the pressure gradient. It should be pointed out that the direction of the pressure gradient is not necessarily parallel to the cell-mean flow direction, owing to the anisotropy of the porous medium, namely the potentially differing values of unit cell dimensions h_{uc} and l_{uc} . The flow in a unit cell is steady and incompressible, has uniform properties, and is governed by the continuity and momentum equations, given below:

Conservation of mass

$$\frac{\partial u}{\partial x} + \frac{\partial v}{\partial y} = 0 \quad (3)$$

x-direction conservation of momentum

$$\rho_f \left(u \frac{\partial u}{\partial x} + v \frac{\partial u}{\partial y} \right) = \beta - \frac{\partial P}{\partial x} + \mu_f \left(\frac{\partial^2 u}{\partial x^2} + \frac{\partial^2 u}{\partial y^2} \right) \quad (4)$$

y-direction conservation of momentum

$$\rho_f \left(u \frac{\partial v}{\partial x} + v \frac{\partial v}{\partial y} \right) = \zeta - \frac{\partial P}{\partial y} + \mu_f \left(\frac{\partial^2 v}{\partial x^2} + \frac{\partial^2 v}{\partial y^2} \right) \quad (5)$$

The boundary conditions are provided by the no-slip requirement on the rods surfaces, given as follows:

$$u = v = 0 \quad (6)$$

At the upstream and downstream ends of the solution domain, shown by the dashed line in Fig. 1 are the periodicity conditions in the x and y directions, respectively

$$\phi(0, y) = \phi(l_{uc}, y) \quad \phi = u, v, P \quad (7)$$

$$\phi(x, 0) = \phi(x, h_{uc}) \quad \phi = u, v, P \quad (8)$$

The flow at a mean angle, α , with respect to the unit cell is established by specifying the unit cell Reynolds number using the superficial velocity and mean flow angle.

The energy equation can be written separately for the incompressible fluid and the solid rods, as:

Fluid phase:

$$\rho_f c_{pf} \left(u \frac{\partial T}{\partial x} + v \frac{\partial T}{\partial y} \right) = k_f \left(\frac{\partial^2 T}{\partial x^2} + \frac{\partial^2 T}{\partial y^2} \right) \quad (9)$$

Solid phase:

$$0 = k_s \left(\frac{\partial^2 T}{\partial x^2} + \frac{\partial^2 T}{\partial y^2} \right) \quad (10)$$

Because of the imposed uniform-flux boundary condition, Eq. (10) and the thermal field within the rods are not needed. Equation (10) is added for completeness and would be needed if the conduction calculations were needed to establish the interfacial boundary conditions.

The periodic boundary condition for the temperature field is also obtained by assuming thermally developed conditions. In the thermally fully developed flow, the thermal energy added within a periodic unit cell will be absorbed by the working fluid. This results in a fixed rise in the bulk temperature of the fluid across each periodic unit cell. The energy balance along the macroscopic flow direction can thus be written

$$\rho_f c_{pf} |\langle \vec{u} \rangle| \frac{d\langle T \rangle^f}{dX} = \dot{S}_{gen} \quad (11)$$

The corresponding boundary conditions that satisfy the macroscopic energy balance for the thermally fully developed flow are imposed as follows:

$$T(l_{uc}, y) = T(0, y) + \left(\frac{\dot{S}_{gen}}{\rho_f c_{pf} |\langle \vec{u} \rangle|} \right) l_{uc} \cos \alpha \quad (12)$$

and

$$T(x, h_{uc}) = T(x, 0) + \left(\frac{\dot{S}_{gen}}{\rho_f c_{pf} |\langle \vec{u} \rangle|} \right) h_{uc} \sin \alpha \quad (13)$$

Details of the numerical procedure utilized in discretization and the solution of the above governing equations can be found in a later numerical procedure section of this paper.

2.2. Thermal dispersion

The following section discusses computation of dispersion for eventual implementation into the porous medium model. At this point, it is instructive to introduce the porous medium model heat transfer equation. Typically, it is that local thermal equilibrium exists between the fluid and solid phases, namely, $\langle T \rangle^f = \langle T \rangle^s = \langle T \rangle$. The fluid phase and solid phase energy equations are added to derive an energy equation for the porous medium as follows:

$$\rho_f c_{pf} \nabla \cdot \langle \vec{u} \rangle \langle T \rangle = \nabla \cdot [\epsilon k_f + (1 - \epsilon) k_s] \nabla \langle T \rangle + \nabla \cdot \mathbf{k}_{dis} \cdot \nabla \langle T \rangle \quad (14)$$

The first term on RHS in the above equation is the Laplacian conduction term; if the thermal conductivity is based on the parallel model. Then the stagnant thermal conductivity is given as $k_{st} \approx \epsilon k_f + (1 - \epsilon) k_s$. A term for tortuosity has been omitted. Kuwahara et al. [25,26] investigated tortuosity and dispersion coefficients. They provide an analytical expression for the tortuosity as a function of medium porosity which is independent of the flow angle and valid in the low Peclet range ($Pe \leq 1$). They show that at high Peclet numbers, dispersion dominates and the tortuosity becomes negligible. Where the thermal dispersion resulting from

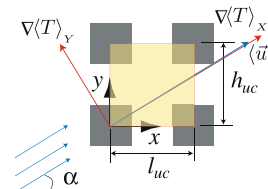


Fig. 2. Linear temperature gradient imposed on an isotropic periodic unit cell (top) and anisotropic unit cell (bottom).

the spatially fluctuations of the velocity and temperature fields is modeled using a gradient type hypothesis as follows:

$$-\rho_f c_{pf} \langle \tilde{T} \tilde{\mathbf{u}} \rangle = \mathbf{k}_{dis} \cdot \nabla \langle T \rangle \quad (15)$$

For the determination of the dispersion, \mathbf{k}_{dis} we follow Arquis et al. [23,24], and impose a linear macroscopic temperature gradient either parallel or perpendicular to a macroscopically flow direction, as shown in Fig. 2. The microscopic temperature field within the unit cell, or REV, is all that is needed to determine the stream-wise and cross-stream dispersions values.

In order to obtain the stream-wise dispersion, the temperature gradient is imposed parallel to the mean velocity vector, as follows:

$$\nabla \langle T \rangle = \frac{\Delta T}{l_{uc}} \cos \alpha \hat{i} + \frac{\Delta T}{h_{uc}} \sin \alpha \hat{j} \quad (16)$$

Therefore, the temperature boundary conditions on the unit cell are imposed as

$$\begin{aligned} T|_{x=l_{uc}} &= T|_{x=0} + \Delta T \cos \alpha \\ T|_{y=h_{uc}} &= T|_{y=0} + \Delta T \sin \alpha \end{aligned} \quad (17)$$

Hence, we obtain the stream-wise dispersion XX component of the dispersion tensor, which is given by

$$k_{XX} = \frac{-\rho_f c_{pf}}{\Delta T l_{uc}} \int_0^{h_{uc}} \int_0^{l_{uc}} (T - \langle T \rangle) (\tilde{u} - \langle \tilde{u} \rangle) dx dy \cdot (\cos \alpha \hat{i} + \sin \alpha \hat{j}) \quad (18)$$

On the other hand, to obtain the cross-stream dispersion component, the temperature gradient is imposed perpendicular to the mean flow, given as

$$\nabla \langle T \rangle = \frac{\Delta T}{l_{uc}} - \sin \alpha \hat{i} + \frac{\Delta T}{h_{uc}} \cos \alpha \hat{j} \quad (19)$$

and the corresponding periodic boundary conditions are

$$\begin{aligned} T|_{x=l_{uc}} &= T|_{x=0} - \Delta T \sin \alpha \\ T|_{y=h_{uc}} &= T|_{y=0} + \Delta T \cos \alpha \end{aligned} \quad (20)$$

where the cross-stream dispersion YY component of the is given as follows:

$$k_{YY} = \frac{-\rho_f c_{pf}}{\Delta T h_{uc}} \int_0^{h_{uc}} \int_0^{l_{uc}} (T - \langle T \rangle) (\tilde{u} - \langle \tilde{u} \rangle) dx dy \cdot (-\sin \alpha \hat{i} + \cos \alpha \hat{j}) \quad (21)$$

2.3. Numerical procedure

In the following section the numerical procedure utilized in discretization and solution of the above governing equations will be explained. The governing equations were solved using the finite-volume procedure described by Patankar [42]. A rectangular grid is used to subdivide the computational domain. A main grid point is located at the center of each control volume. Grid point values of the scalar variables, such as temperature and pressure, are stored at the main grid points. A staggered grid is used to locate velocity components at the faces of the control volumes. Discretization equations for the discrete values of the variables are constructed by integrating the corresponding conservation laws over the appropriate control volumes. The power-law differencing scheme is used to obtain the combined convection–diffusion coefficients and the *SIMPLER* algorithm of Patankar [43] is used to handle the velocity–pressure coupling. In the present study, the solution of the flow field is carried out first, followed by a solution of the temperature field since the fluid properties are assumed to be independent of temperature. The *SIMPLER*

algorithm of Patankar [43] is utilized to solve the momentum and continuity discretization equations. A procedure for computation of the flow field for a specified mass flow rate through the unit cell, which was proposed by Sathyamurthy and Karki [44], has been modified for the angled flow and has been incorporated into the overall solution algorithm, as described below. The dimensional form of the discretization momentum equations in the x and y directions can be written as:

$$a_P u_P = \sum_{nb} a_{nb} u_{nb} + A(P_P - P_E) + \beta \Delta V \quad (22)$$

and

$$a_P v_P = \sum_{nb} a_{nb} v_{nb} + A(P_P - P_N) + \zeta \Delta V \quad (23)$$

A special feature of these equations is the appearance of the pressure forces due to the constant pressure gradients β and ζ which determine the flow rate through the unit cell. The calculation of the flow field for a given value of β and ζ can be carried out in a straightforward manner. However, in most practical situations, it is of interest to compute the flow characteristics for a given flow rate through the unit cell rather than for a given pressure gradient. This corresponds to a specified Reynolds number of the flow and a specific flow angle. A procedure for adjustment of the pressure gradients, β and ζ , proposed by Kelkar and Patankar [45] has been modified for periodically angled flow. It is assumed in each iteration of the *SIMPLER* algorithm that the discretized equations are nominally linear. Thus, the non-linear coefficients are computed using the approximate velocity field. For a linear problem, the through flows in the x and y directions are directly proportional to the pressure gradients, β and ζ , respectively. This property provides the motivation for the following manner of adjusting the values β and ζ at the end of each iteration as follows:

$$\beta = \beta^* \eta^\omega \quad \eta = \frac{u_{av}}{u_{av}^*} \quad (24)$$

and

$$\zeta = \zeta^* \lambda^\omega \quad \lambda = \frac{v_{av}}{v_{av}^*} \quad (25)$$

Here, u_{av} and v_{av} are the desired average velocity components of the flow through the unit cell and u_{av}^* and v_{av}^* are the average velocity components of the available flow field at each iteration, which correspond to the pressure gradients β^* and ζ^* . The exponent $\omega \leq 1$ serves as an under-relaxation factor to ensure convergence. Further, the velocity field is updated with each adjustment in β and ζ as follows:

$$u = u^* \eta \quad (26)$$

and

$$v = v^* \lambda \quad (27)$$

Since adjustment of the velocity in Eqs. (26) and (27) involves the multiplication of the velocity field obtained after the solution of the velocity correction equation, the corrected velocity field also satisfies continuity. Each iteration of the overall solution algorithm for the flow field consists of an iteration of the *SIMPLER* algorithm followed by an adjustment of the pressure gradients, and the velocity field, according to Eqs. (24) and (25).

The solution of each linear set of algebraic discretized equations is accomplished using the line-by-line method of Patankar [46]. A cyclic, *Tri-Diagonal Matrix Algorithm (CTDM)* is modified for the double-periodic domain. To enhance convergence, a block-correction procedure, described by Patankar [46], is modified for a domain periodic in both directions and is incorporated in the overall solution algorithm.

The solution of the periodically fully-developed temperature field is carried out without its decomposition into a periodic and linear part. However, the discretization procedure must incorporate the condition that the temperature of the fluid rises by a fixed amount across the unit cell and must satisfy the macroscopic energy balance, as given by Eq. (11). For this purpose, the procedure proposed by Kelkar and Patankar [45] has been modified for the angled flow. In this procedure, discretization of the energy equation is carried out in the usual fashion, in terms of dimensional temperature, and the periodic conditions given by Eqs. (28) and (29)

$$T(l_{uc}, y) = T(0, y) + \left(\frac{\dot{S}_{gen}}{\rho_f c_{pf} |\langle \vec{u} \rangle|} \right) l_{uc} \cos \alpha \quad (28)$$

$$T(x, h_{uc}) = T(x, 0) + \left(\frac{\dot{S}_{gen}}{\rho_f c_{pf} |\langle \vec{u} \rangle|} \right) h_{uc} \sin \alpha \quad (29)$$

These conditions are incorporated directly into the discretization of the temperature at the grid points that are adjacent to the periodic boundaries. Fig. 3 represents periodic boundaries along the x-direction. The discretization equation for the dimensional temperature at the main grid point 1, next to the left periodic boundary, is as follows:

$$a_p T_1 = \sum_{nb \neq 1-} a_{nb} T_{nb} + a_w T_{1-} + b \quad (30)$$

Note that the west neighbor T_{1-} , falls outside the domain. It can be related to the temperature T_n at the corresponding point in the domain to the right periodic boundary using the periodic boundary condition given by Eq. (28) as follows:

$$T_{1-} = T_n - (\Delta T)_x \quad (31)$$

where $(\Delta T)_x$ is defined in terms of Eq. (28) which is given by

$$(\Delta T)_x = \frac{\dot{S}_{gen} l_{uc} \cos \alpha}{\rho_f c_{pf} |\langle \vec{u} \rangle|} \quad (32)$$

Hence, the discretization equation given by Eq. (30) can be re-written as follows:

$$a_p T_1 = \sum_{nb} a_{nb} T_{nb} + (b - a_w (\Delta T)_x) \quad (33)$$

The sum over the neighbors now includes the periodic neighbor T_n of the temperature T_1 . Similarly, the discretization equation for the grid point temperature T_n can be derived in an identical manner, as follows:

$$a_p T_n = \sum_{nb} a_{nb} T_{nb} + (b + a_e (\Delta T)_x) \quad (34)$$

The equations for the y direction are derived similarly and given as follows:

$$a_p T_1 = \sum_{nb} a_{nb} T_{nb} + (b - a_s (\Delta T)_y) \quad (35)$$

and

$$a_p T_n = \sum_{nb} a_{nb} T_{nb} + (b + a_n (\Delta T)_y) \quad (36)$$

where $(\Delta T)_y$ is defined in terms of Eq. (29) which is given by

$$(\Delta T)_y = \frac{\dot{S}_{gen} h_{uc} \sin \alpha}{\rho_f c_{pf} |\langle \vec{u} \rangle|} \quad (37)$$

The system of equations now contains only grid point temperatures within a periodic unit cell and can now be solved. The method outlined above is employed to predict the flow and heat transfer in the geometry shown in Fig. 1. Computation is first carried out for the isotropic configuration corresponding to $h_{uc}/l_{uc} = 1$, $d_{uc}/l_{uc} = 1/2$, which leads to a volumetric porosity, $\epsilon_v = 0.75$, at Reynolds numbers $1-10^3$ and flow angles, α , from 0° to 90° . The Reynolds number is based on the absolute value of the Darcian velocity, and the longitudinal center-to-center distance, hence taking the form $Re_{uc} = |\langle \vec{u} \rangle| l_{uc} / \nu_f$. Since the volumetric porosity is defined as $\epsilon_v = 1 - (d_{uc}^2 / h_{uc} l_{uc})$, Re_{uc} can be related to the Reynolds number based on the size of the rod, d_{uc} , such that $Re_{duc} = |\langle \vec{u} \rangle| d_{uc} / \nu_f = Re_{uc} ((1 - \epsilon_v) h_{uc} / l_{uc})^{1/2}$. Here, an isotropic case and two degrees of anisotropy are investigated by setting the geometric parameter h_{uc}/l_{uc} to $3/2$ and 2 , which corresponds to volumetric porosities of $\epsilon_v = 0.833$ and $\epsilon_v = 0.875$, respectively. The iterative solution of the coupled continuity and momentum equations is terminated when the sums of the absolute values of the mass and momentum residuals at each internal grid point, normalized by incoming mass and momentum fluxes, fall below 0.01%, and when the maximum changes of the average pressure gradients, and the maximum changes in the average velocity components do not exceed 10^{-5} during an iteration. The temperature field is considered to be converged when the overall heat balance is within $10^{-3}\%$ and when the maximum changes in the Nusselt numbers do not exceed 10^{-5} during an iteration. Table 1 shows the predicted values of the dimensionless pressure gradient, $(\partial \langle P \rangle^f / \partial X) / (\rho_f |\langle \vec{u} \rangle|^2 l_{uc})$ on the three grids considered. The computed values of $(\partial \langle P \rangle^f / \partial X) / (\rho_f |\langle \vec{u} \rangle|^2 l_{uc})$ on the 40×40 grid differ by less than 3% from those on the 60×60 grid; the results on the 60×60 grid were within 0.5% of those on the 80×80 grid. These results indicated that the numerical solutions on the 80×80 grid were adequate for the study.

3. Results and discussion

3.1. Flow resistance

In this section we shall give the results obtained by conducting the flow and heat transfer and the dispersion analyses. The results of the computations of the flow field are first discussed, followed by a discussion of the periodically fully-developed temperature field. For clarity, both the velocity vector plots and the temperature

Table 1
Effect of grid refinement on the dimensionless pressure gradient.

Re_{uc}	Flow angle	40×40 grid	60×60 grid	80×80 grid
10	0	7.44	7.66	7.70
10^2	0	0.797	0.820	0.823
10^3	0	0.0853	0.0878	0.0882
10	45	7.97	8.16	8.20
10^2	45	2.65	2.71	2.72
10^3	45	3.07	3.15	3.16

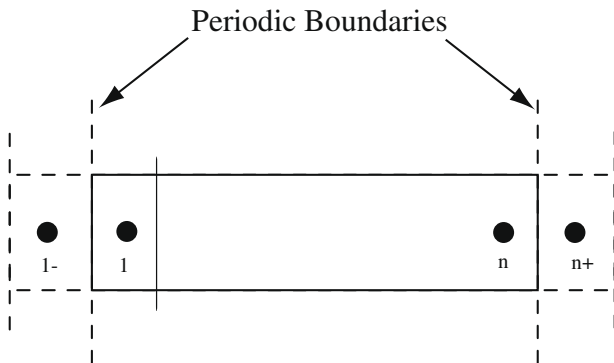


Fig. 3. A schematic showing scalar control volumes bordering periodic boundaries.

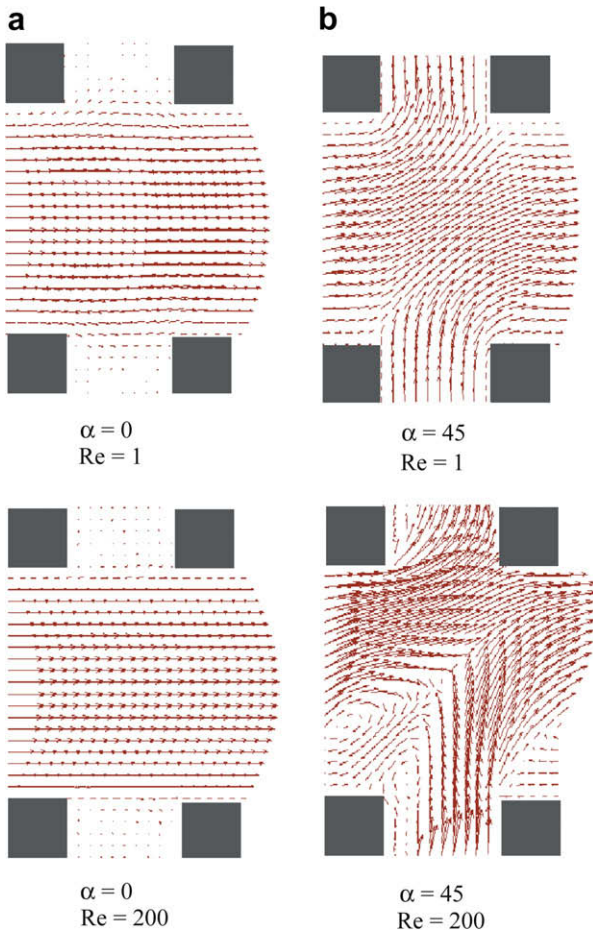


Fig. 4. Velocity vectors $h_{uc}/l_{uc} = 1.5$: (a) $\alpha = 0^\circ$ and (b) $\alpha = 45^\circ$.

contours are plotted on a grid that is coarser than that used in the computations. In this study we investigated three array arrangements by varying the unit cell aspect ratio. The three aspect ratios h_{uc}/l_{uc} used are 1, 1.5, and 2 they correspond to a volumetric porosity, ϵ of 0.75, 0.833, and 0.875, respectively. Where the volumetric porosity is defined as the volume fraction of fluid-occupied space in the unit cell. Fig. 4 shows the velocity vectors in the periodic unit cell for the array having an aspect ratio, h_{uc}/l_{uc} of 1.5, for flow angles, $\alpha = 0^\circ$ and $\alpha = 45^\circ$ and Reynolds numbers, Re_{uc} , of 1 and 200. For the cases of $\alpha = 0^\circ$ and $Re_{uc} = 1$ and 200, the regions between the rods, along the transverse direction, are completely occupied by recirculating flow, which is very weak compared to the throughflow. Thus, the fluid is effectively flowing through a channel of height ($h_{uc} - d_{uc}$ see Fig. 1). Based on the lack of flow recirculation, it can be inferred from Fig. 4 (a) that the viscous force contribution to the pressure drop predominates over the inertial contribution. For the case of $\alpha = 45^\circ$ and $Re_{uc} = 1$ and 200 shown in Fig. 4(b), the flow resistance is mainly due to viscous effects. However, as the Reynolds number increases to $Re_{uc} = 200$, strong recirculation in the vicinity of the leeward surfaces of the rods suggests that inertial contributions may dominate the viscous effects. This will be quantified later. Hence, at higher Reynolds numbers, form drag becomes the main contributor to the flow resistance. To examine the relative roles of viscous and inertial forces, we define the apparent permeabilities, which vary with the direction of the flow through the porous medium. The apparent permeability is a measure of the medium's ability to transmit fluids. Plotted in Fig. 5 are curves of

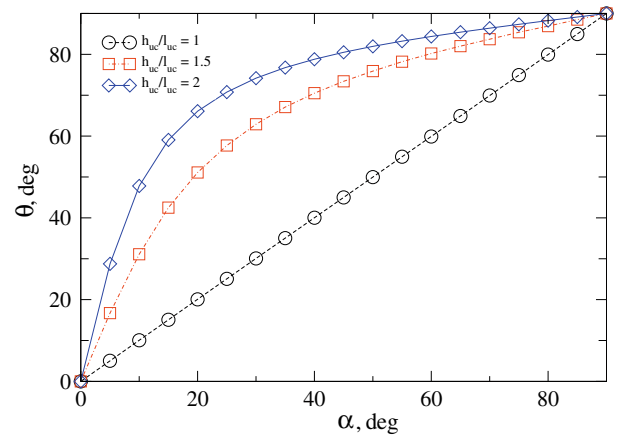


Fig. 5. Pressure gradient angle vs. mean flow angle, for Darcy flow, $Re_{uc} = 1$.

the pressure gradient angles versus the mean flow angle. The $h_{uc}/l_{uc} = 1$ line is linear from 0° to 45° , indicating that the vectors $\langle \vec{u} \rangle$ and $-\langle \frac{\partial P}{\partial X} \rangle$ are aligned with one another. However the non-linearity of the two other curves which corresponds to the unit cells $h_{uc}/l_{uc} = 1.5$ and $h_{uc}/l_{uc} = 2$, respectively; are the result of the anisotropy of those arrays.

In the anisotropic media corresponding to arrays with geometric ratios of $h_{uc}/l_{uc} = 1.5$ and 2, the vectors $\langle \vec{u} \rangle$ and $-\langle \frac{\partial P}{\partial X} \rangle$ are non-colinear, except when flow is in the direction of one of the principal axes, $\alpha = 0^\circ$ and $\alpha = 90^\circ$. Hence, it is necessary to investigate flows of various directions to determine the directionally dependent permeability. Following Dullien [47] for an orthotropic porous medium, such as shown in Fig. 1, and for low Reynolds number flows ($Re_{uc} \leq 1$), Darcy's law governs the flow, as follows:

$$-\frac{\partial \langle P \rangle^f}{\partial X} = \frac{\mu_f}{K_{fn}} |\langle \vec{u} \rangle| \quad (38)$$

Next, the directional permeability, K_{fn} , is written in terms of the macroscopic (or cell averaged) flow. In Eq. (38), the directional permeability, K_{fn} , measured along the macroscopic flow direction, X , is defined as follows:

$$K_{fn} = \left[\frac{\cos^2 \alpha_1}{K_1} + \frac{\cos^2 \alpha_2}{K_2} \right]^{-1} \quad (39)$$

where the angles α_1 and α_2 are the direction cosines of the macroscopic velocity vector. For the particular rod arrangements on hand, the directional permeability is given by in terms of mean flow angle, α_1 , as

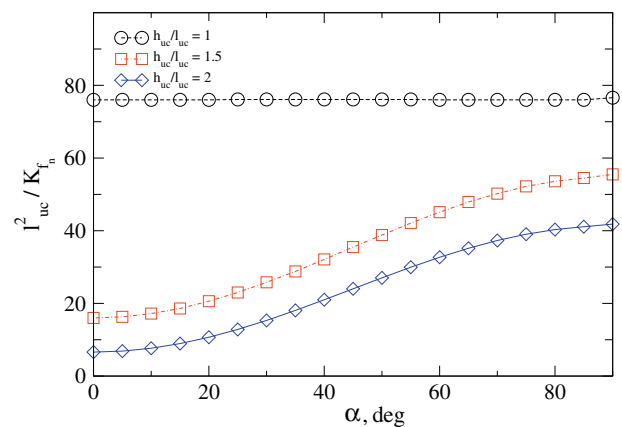


Fig. 6. Directional permeability at $Re_{uc} = 1$.

$$K_{fn} = \left[\frac{\cos^2 \alpha}{K_1} + \frac{\sin^2 \alpha}{K_2} \right]^{-1} \quad (40)$$

The directional permeability values, K_{fn} , for the three sets of media configurations are obtained according to Eq. (40) and are plotted in Fig. 6 and are in agreement of the findings of Nakayama et al. [40].

It must be noted that the permeability values for the isotropic array $h_{uc}/l_{uc} = 1$, are independent of flow angle, since the mean angle of the flow and the mean angle of the pressure gradient are aligned. The mean pressure gradient applied to the unit cell is proportional to the Darcy velocity through the unit cell (pressure forces are balanced by viscous forces). In this limiting case, Darcys law governs the flow field. However, the permeability values for the two anisotropic arrays are inversely proportional to the mean flow angles. The directional permeability minimum and maximum values correspond to the two principal permeabilities computed with the incoming flow at $\alpha = 90^\circ$ and 0° , respectively. The maximum permeability corresponds to the least flow blockage, as attained with an incoming flow angle of α of 0° . At Reynolds numbers, $Re_{uc} > 10$ the inertial effects become significant and, even for an isotropic medium, the mean velocity vector and pressure gradient are non-colinear, as shown in Fig. 7

Hence, the pressure gradient angle variations with flow angle for the three array types follow similar trends. It is interesting to note that the degree of anisotropy effect becomes less apparent when the inertial effects dominate the flow characteristics. Furthermore, when the mean flow angle, α , is in the range of 20° – 55° , the pressure gradient is imposed at a nearly uniform angle of $\sim 40^\circ$ as seen in Fig 7. The extent and location of the circulation zones for these flows are similar to one another and the effective openness of the array to flows around the recirculation zone is relatively invariant with flow angle. However, for flows with mean flow angles in the range 5° – 15° and 65° – 90° , the least resistance paths would be along the principal axes, which are effectively channel flows of width $h_{uc} - d_{uc}$ and $l_{uc} - d_{uc}$. Therefore, the pressure gradient must be imposed at a steeper mean angle relative to the corresponding principal flow direction. As the flow Reynolds number is increased the inertial effects become significant. Darcy's law based on a balance a of viscous force and pressure gradient is no longer valid. The inertial contribution due to separation and a wake around the porous structure are accounted for via the Forchheimer-extended Darcy law. At high Reynolds numbers, the Forchheimer term governs the flow. This term in the Darcy law expression is

$$-\frac{\partial \langle P \rangle^f}{\partial X} = \rho_f b_{fn} |\langle \vec{u} \rangle|^2 \quad (41)$$

The Forchheimer coefficient, b_{fn} , is the asymptotic value of the dimensionless pressure gradient

$$b_{fn} = - \left(\frac{\partial \langle P \rangle^f}{\partial X} \right) \left(\frac{l_{uc}}{\rho_f |\langle \vec{u} \rangle|^2} \right) \quad (42)$$

in the limit of very large Reynolds numbers. The directional Forchheimer coefficient verses flow angle is as shown in Fig. 8 and these are also in good agreement of the findings of Nakayama et al. [40].

Here, the Forchheimer coefficient attains its lowest values along the principal directions and reaches a maximum value when the flow angle, α , is 45° (i.e. $h_{uc}/l_{uc} = 1$). The maximum point shifts (see Fig. 8) with increasing anisotropy of the rod arrays (i.e. $h_{uc}/l_{uc} = 1.5$, $h_{uc}/l_{uc} = 2$). The Forchheimer coefficient results are in good agreement with those obtained by Nakayama et al. [40]. It must be noted that for the anisotropic media cases $h_{uc}/l_{uc} = 1.5$ and $h_{uc}/l_{uc} = 2$ the inertial coefficient attains a maximum plateau in the flow angle range of 45° – 60° and 45° – 70° , respectively. The increase in the inertial coefficient is a result of the “openness” of the array to the approaching flow within these angle ranges. In other-word, if we consider an inertial flow with 0° approach angle then the flow is very much like a channel flow within the gap between the cylinders, while the within-cylinder space is completely filled with recirculating fluid. Now, an increase in the approach angle will result in an additional path available for the flow and two standing vortices behind the solid at the SW corner to the unit cell. On the west face of the unit cell the “west” flow goes through a region on top of standing eddie and the “south” flow goes through a region to the right of the other standing eddie. Further increase of approach angle will result in shifting of the “west” flow to “south” flow and also a shift in standing eddies location. Within the forementioned angle ranges above the net flow and the resulting pressure drop is nearly constant. Hence, the plateau in the inertial coefficient.

For finite Reynolds number flows, such as those in this study, it would be convenient to cast the flow resistance values in terms of apparent permeability. The concept of apparent permeability was first introduced by Edwards et al. [5]. Since the apparent permeability is a function of Reynolds number, it accounts for both the viscous and inertial effects. The principal apparent permeabilities, \tilde{K}_{XX} and \tilde{K}_{YY} , are defined as:

$$\tilde{K}_{XX} = \frac{\mu_f |\langle \vec{u} \rangle|}{\nabla P_X} \quad (43)$$

and

$$\tilde{K}_{YY} = \frac{\mu_f |\langle \vec{u} \rangle|}{\nabla P_Y} \quad (44)$$

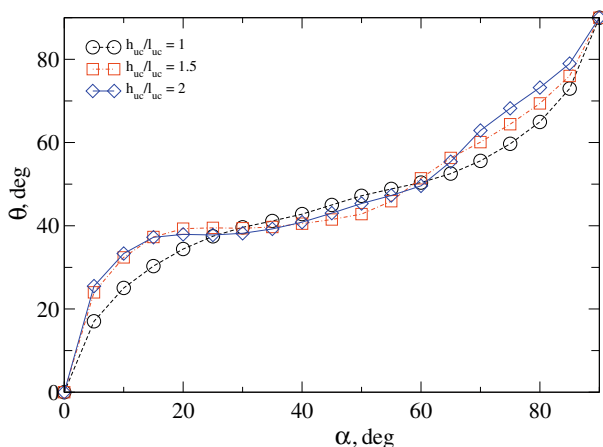


Fig. 7. Pressure gradient angle vs. mean flow angle, inertial flow, $Re_{uc} = 200$.

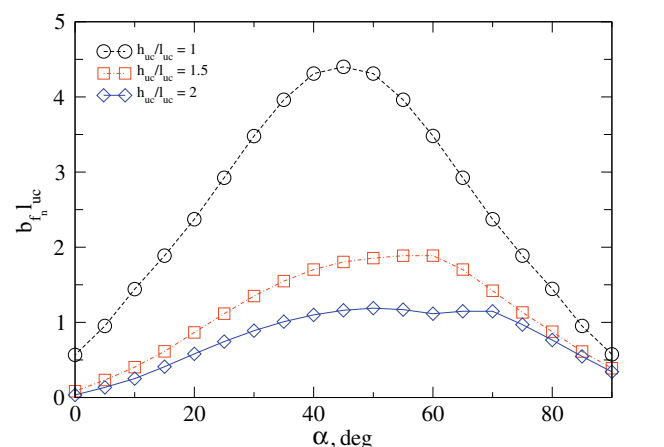


Fig. 8. Directional Forchheimer coefficient.

The above apparent permeability is utilized to establish a relationship between the mean velocity and the macroscopic pressure gradient. The apparent permeability is dependent on the orientation of the applied pressure gradient. This is due to the non-linearities within the local fluid motion. In contrast, the true permeability is representative of average material properties. A data base of apparent permeabilities, \tilde{K}_{XX} and \tilde{K}_{YY} , was generated for ranges of flow angles, Reynolds numbers, and geometries of the present study. The data base was utilized for closure of a macroscopic analysis. Fig. 9 shows examples of, normalized permeabilities, \tilde{K}_{XX} and \tilde{K}_{YY} , versus Reynolds number at angles $\alpha = 0^\circ$ and 45° .

The apparent permeability, \tilde{K}_{XX} , for flow at an angle, α , of 0° does not vary much with Reynolds number; the flow along a principal direction is similar to fully-developed duct flow. If the flow is at an angle, α , of 45° , the recirculation zones within the unit cell increase with increasing Reynolds number and the effective area open to flow is decreased. This is evident in the stream function plots shown in Fig. 10.

Consequently, the apparent permeability diminishes with increasing Reynolds number. For the isotropic array case at a given mean flow angle, α , of 45° the permeabilities, \tilde{K}_{XX} and \tilde{K}_{YY} , are identical. However, \tilde{K}_{XX} is less than \tilde{K}_{YY} for anisotropic arrays such as $h_{uc}/l_{uc} = 1.5$ and 2.

3.2. Interfacial heat transfer coefficient

The heat transfer in the periodically fully-developed flow is characterized using a Nusselt number averaged over the unit cell, which is defined as

$$\langle Nu \rangle_{uc} = \frac{h_{sf} l_{uc}}{k_f} \quad (45)$$

The average interfacial heat transfer coefficient is defined as

$$h_{sf} = \frac{\frac{1}{V_{REV}} \int_{A_{sf}} \vec{n}_{sf} \cdot k_f \nabla T_f dA}{\langle T_s \rangle^s - \langle T_f \rangle^f} \quad (46)$$

where A_{sf} is the interfacial area between the rod surface and the fluid. Whereas, $\langle T_s \rangle^s$ and $\langle T_f \rangle^f$ are intrinsic average temperatures of the solid and fluid in the unit cell, respectively. Fig. 11 shows the isotherm distribution in the periodic unit cell for the array $h_{uc}/l_{uc} = 1.5$.

The cases with flow angles, $\alpha = 0^\circ$ and $\alpha = 45^\circ$ at Reynolds numbers, $Re_{luc} = 1$ and $Re_{luc} = 200$, correspond to the velocity fields shown in Fig. 4. For the cases, $\alpha = 0^\circ$ and 45° and $Re_{luc} = 1$, the isotherms are typical of thermal conduction. For the case of $\alpha = 0^\circ$

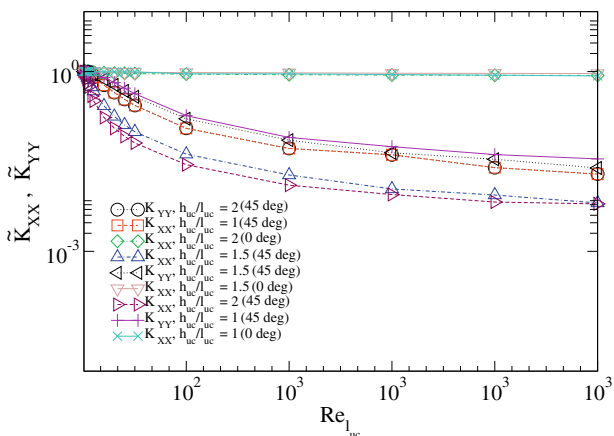


Fig. 9. Normalized apparent permeability, \tilde{K}_{XX} and \tilde{K}_{YY} for flow angle $\alpha = 0^\circ$ and $\alpha = 45^\circ$.

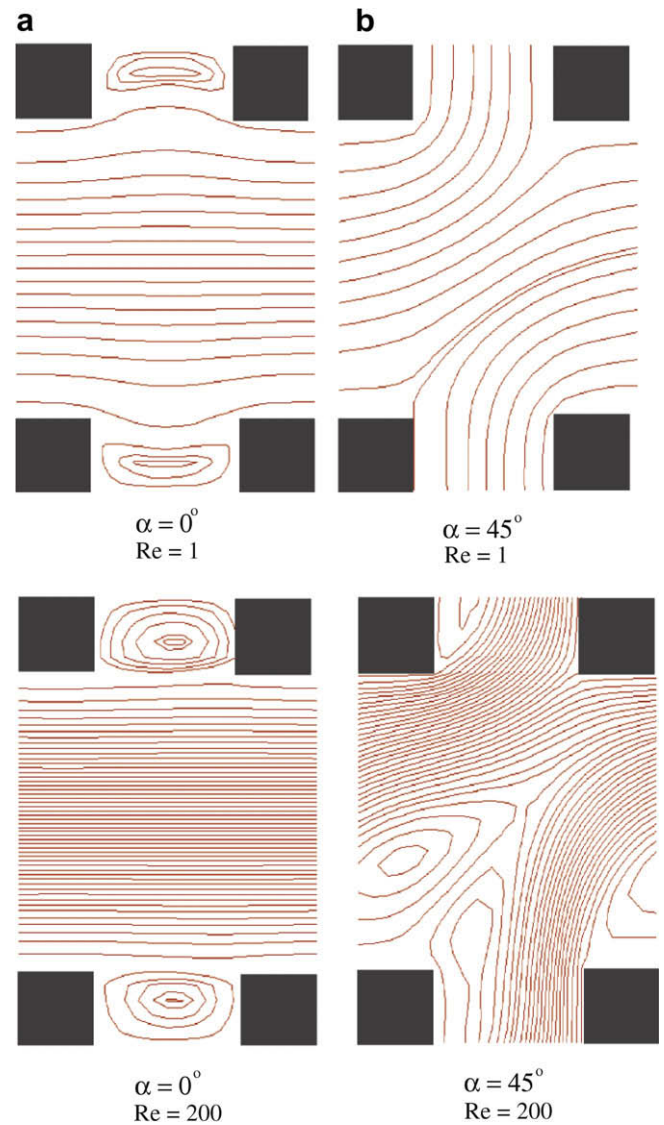


Fig. 10. Stream-function plots for the anisotropic medium case, $h_{uc}/l_{uc} = 1.5$: (a) $\alpha = 0^\circ$ and (b) $\alpha = 45^\circ$.

and $Re_{luc} = 200$, the temperature gradients are steep on the surfaces of the rods and the normal to the surface points in the y -direction. The steep gradients lead to higher heat transfer rates from these surfaces. For the case of $\alpha = 45^\circ$ and $Re_{luc} = 200$, temperature gradients are steep on the upwind (or windward) surfaces of the rods. This is evident by the thin boundary layers and the steep gradients on these surfaces, in comparison with the thicker boundary layers on the downwind (or leeward) sides of rods. The predicted temperature fields conform to the velocity fields presented in Fig. 4, which show that the windward surfaces of the rods are completely washed by the cooling fluid.

The interfacial heat transfer coefficient results for three array configurations are presented in Figs. 12 and 13. The uniform flux condition is applied. It is noted that when the flow is along the principal x -axis, the $\langle Nu \rangle_{uc}$ number increases only slightly with Reynolds number. Since the flow is similar to duct flow, the $\langle Nu \rangle_{uc}$ number is nearly independent of Reynolds number. Conversely, when the flow is at an angle of $\alpha = 45^\circ$, the $\langle Nu \rangle_{uc}$ number increases strongly with Reynolds number. This is more like a wedge flow solution since the most effective heat transfer is on the leading edge. For these cases, the temperature field becomes more complex and the heat transfer is enhanced, as evident in

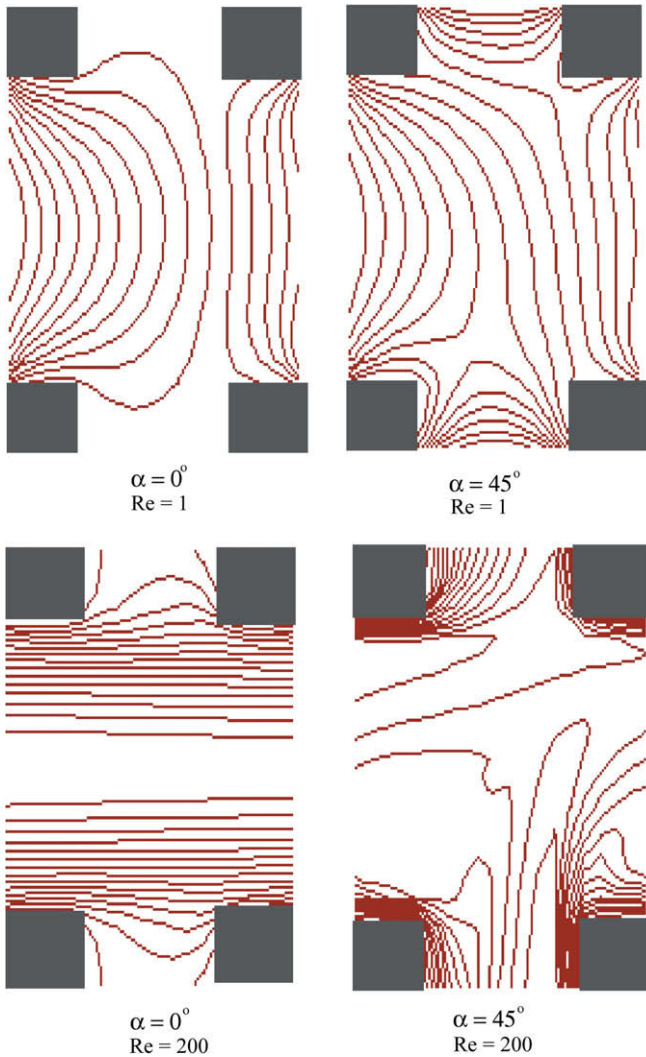


Fig. 11. Isotherms, $h_{uc}/l_{uc} = 1.5$: (a) $\alpha = 0^\circ$ and (b) $\alpha = 45^\circ$.

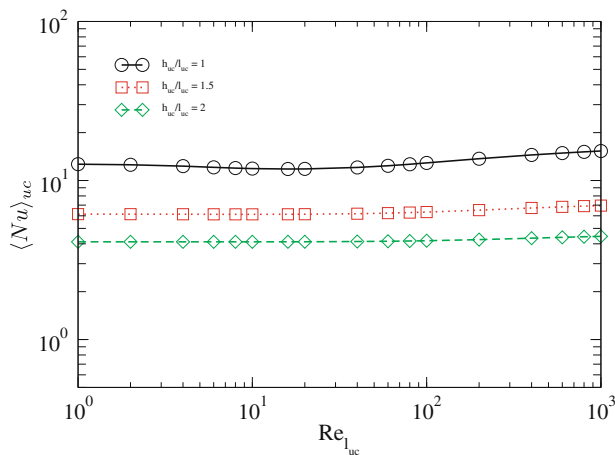


Fig. 12. Nusselt number, $\alpha = 0^\circ$.

the isotherm pattern shown in Fig. 11. Additionally, Fig. 11 conveys that as the Reynolds number increases, the $\langle Nu \rangle_{uc}$ number becomes less sensitive to the anisotropy of the array. This is due to the aforementioned mixing.

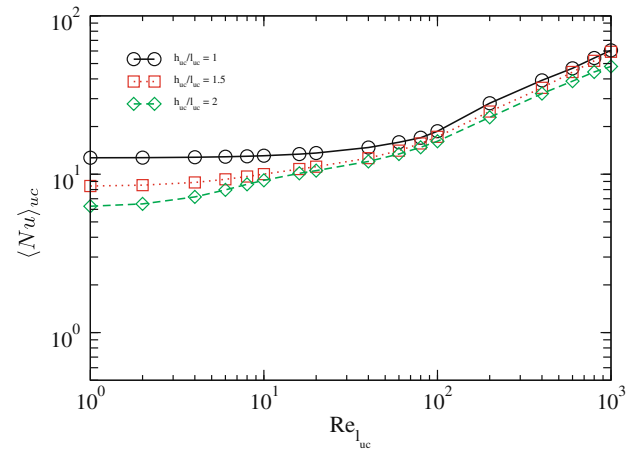


Fig. 13. Nusselt number, $\alpha = 45^\circ$.

3.3. Thermal dispersion

Dispersion in porous media is a phenomenon comprised of both molecular diffusion and spatial velocity deviations from the average Darcy velocities at the pore scale. It is the presence of velocity and temperature gradients at the pore scale in conjunction with application of the volume averaging theorem which gives rise to inclusion of the pore-level conduction–convection contribution or thermal dispersion. Thermal dispersion is essentially the influence of the velocity non-uniformities, at the pore-scale, on the temperature field. Firstly, at pore-scale the dispersion coefficients are determined using a unit cell computation. Secondly, in the system scale computations the dispersion effects are modeled as an additional diffusion mechanism, where the diffusion coefficients are those obtained from the pore-scale computations.

Here, we will compute the dispersion coefficients of the spatially periodic, two-dimensional, porous medium, by varying the porosity, the direction of the mean velocity relative to the unit cell axes, and the Péclet number. Figs. 14 and 15 show typical temperature fields that are obtained at $\alpha = 0^\circ$ and 45° for the two different Reynolds numbers, $Re_{luc} = 1$ and 200. We can see in Fig. 14 that the isotherms are considerably distorted in the flow direction. That is, the temperature field is significantly influenced by throughflow since the macroscopic temperature gradient is imposed parallel to the flow direction. On the other hand, Fig. 15 shows that when the macroscopic temperature gradient is imposed perpendicular to flow direction, the isotherms are also distorted, but not significantly. In other words, stream-wise mechanical dispersion is much greater than cross-stream dispersion since it is driven by the flow. Cross-stream dispersion is weak and is due mainly to flow recirculation.

The stream-wise and cross-stream dispersion coefficients for the various microscopic geometries are given in Figs. 16–22. Fig. 16 is the stream-wise dispersion plotted against the Péclet for various flow angles. It must be noted that the stream-wise dispersion for an isotropic porous medium follows the correlations proposed in [25] with a quadratic Péclet number dependence for low Péclet ($Pe_{luc} \leq 10$) and a linear Péclet number for higher Péclet or ($Pe_{luc} > 10$) and the dispersion coefficient is higher for the flow angle of zero in comparison with other flow angle, the enhancement of stream-wise dispersion may be attributed to increased dispersion of thermal energy in the recirculating fluid regions between the solids. The cross-stream dispersion coefficient is shown in Fig. 17 and follows the linear Péclet dependence proposed by [25] except for the flow angle of zero which was not investigated in [25]. It must be mentioned that the stream-wise

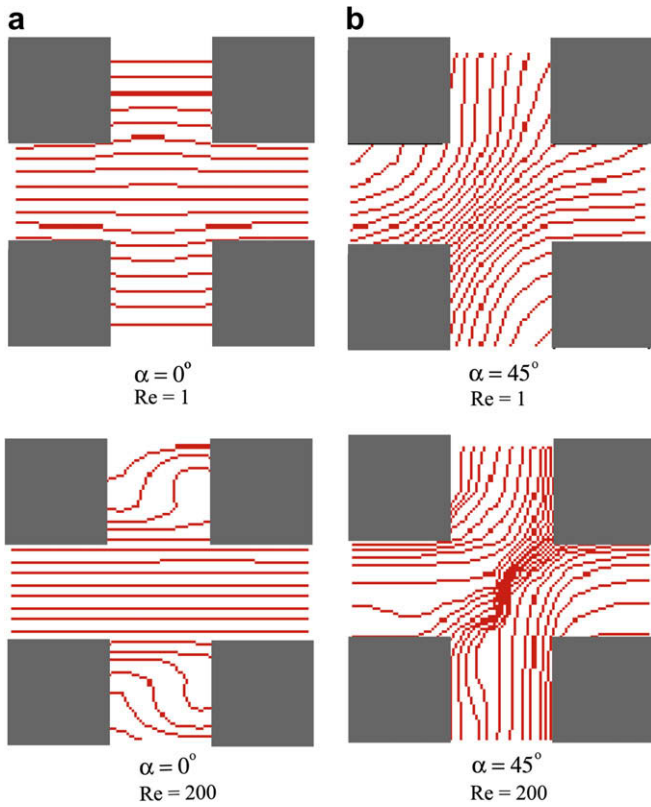


Fig. 14. Temperature gradient is perpendicular to flow direction: the two top unit cells $Re_{luc} = 1$ and flow angle, $\alpha = 0^\circ$ and 45° , the two bottom unit cells $Re_{luc} = 200$ and flow angle, $\alpha = 0^\circ$ and 45° .

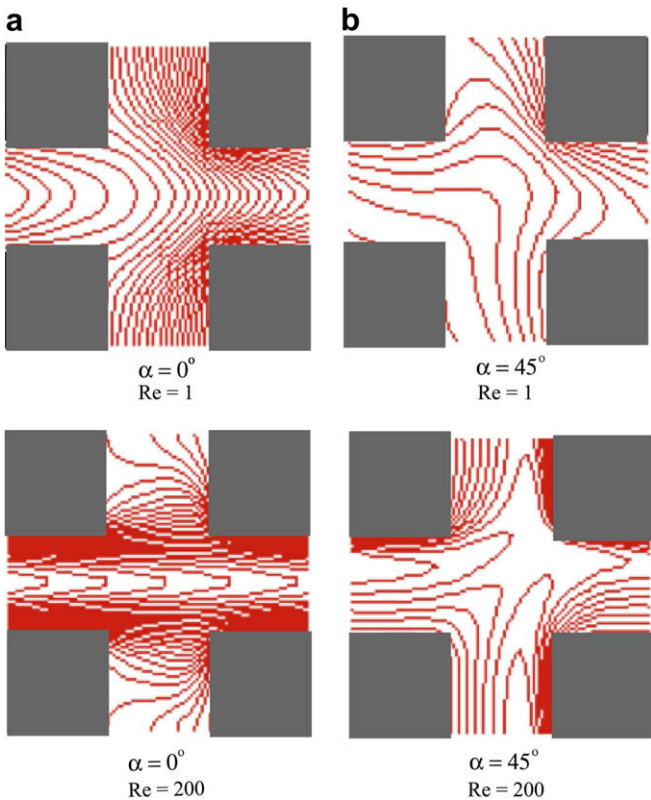


Fig. 15. Temperature gradient is parallel to flow: the two top unit cells $h_{uc}/l_{uc} = 10$ and flow angle, $\alpha = 0^\circ$ and 45° , the two bottom unit cells $h_{uc}/l_{uc} = 200$ and flow angle, $\alpha = 0^\circ$ and 45° .

dispersion for a given Péclet is much greater than the cross-stream dispersion. Fig. 18 shows that total stream-wise dispersion, where the total dispersion is defined as the sum of the both dispersion coefficient and molecular diffusion, the for and isotropic dispersion

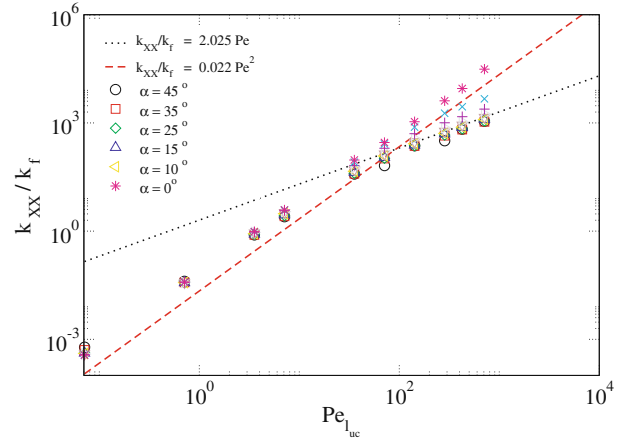


Fig. 16. Stream-wise dispersion coefficient for unit cell $h_{uc}/l_{uc} = 1$, $\alpha = 0^\circ$ – 45° .

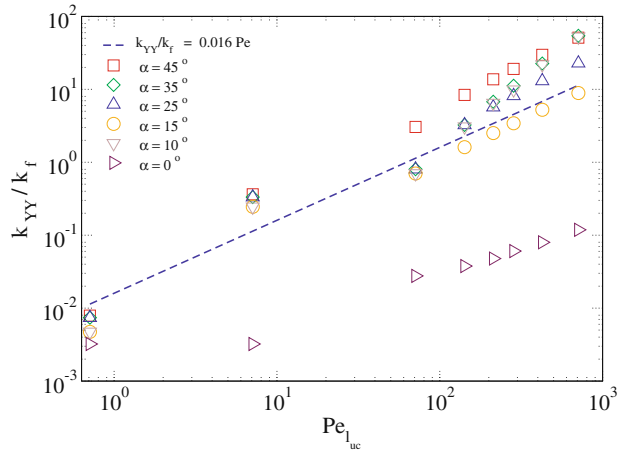


Fig. 17. Cross-stream dispersion coefficient for unit cell $h_{uc}/l_{uc} = 1$, $\alpha = 0^\circ$ – 45° .

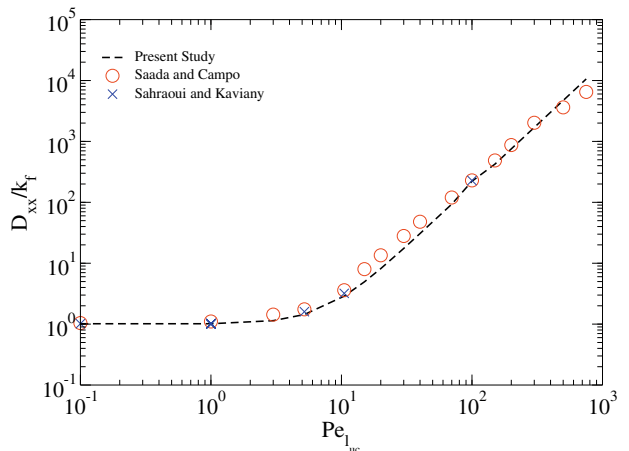


Fig. 18. Stream-wise dispersion coefficient for unit cell $h_{uc}/l_{uc} = 1$ and porosity, ϵ of 0.64 for on-axis flow, $\alpha = 0^\circ$.

is in good agreement with the results given [48] and [49]. Figs. 19–22 show stream-wise and cross-stream dispersion the for the two

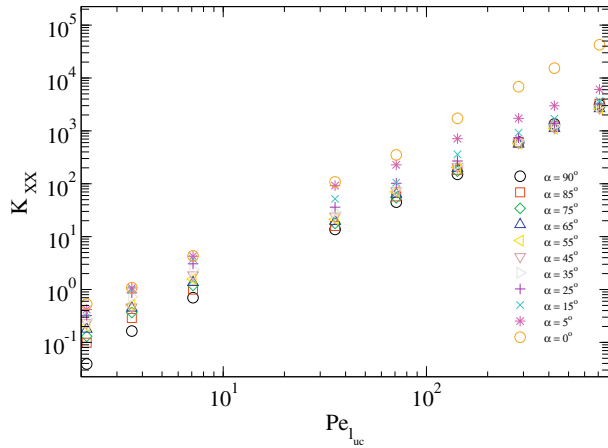


Fig. 19. Stream-wise dispersion coefficient for unit cell, $h_{uc}/l_{uc} = 1.5$, flow angle, $\alpha = 0^\circ - 90^\circ$.

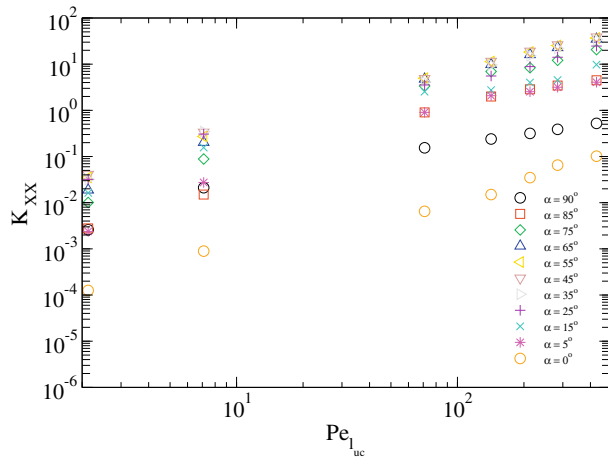


Fig. 20. Cross-stream dispersion coefficient for unit cell, $h_{uc}/l_{uc} = 1.5$, flow angle, $\alpha = 0^\circ - 90^\circ$.

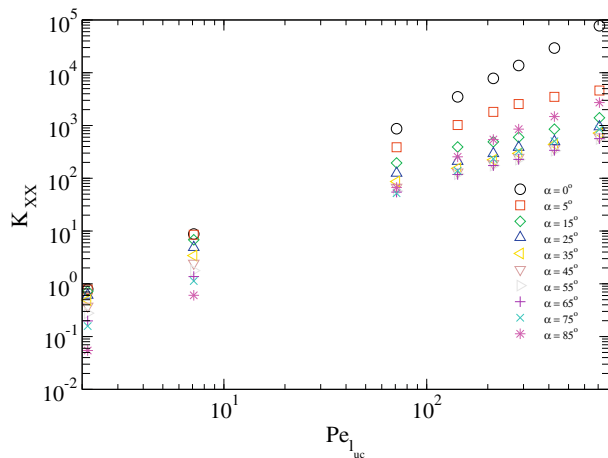


Fig. 21. Stream-wise dispersion coefficient for unit cell, $h_{uc}/l_{uc} = 2$, flow angle, $\alpha = 0^\circ - 90^\circ$.

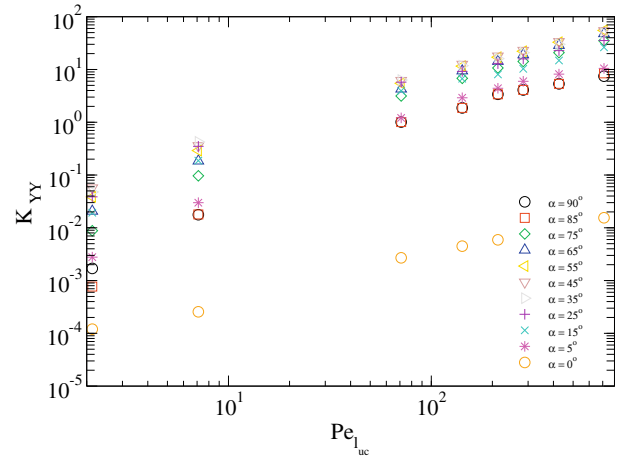


Fig. 22. Cross-stream dispersion coefficient for unit cell, $h_{uc}/l_{uc} = 2$, flow angle, $\alpha = 0^\circ$ and 90° .

anisotropic geometries which correspond a medium porosity of 0.833 and 0.875. Similar patterns in the dispersion coefficients to those observed in the isotropic medium can also be observed here for case of anisotropic geometries. It is noteworthy that dispersion coefficients are not vary monotonically with flow angle which may be attributed to combined effects of the media asymmetry and anisotropy of approaching flow.

4. Unsteady fluid flow

Thus far in this paper the transport properties of the porous media were obtained via unit cell computations assuming steady flow. Mainly, the flow and the heat transfer resistances as well as the thermal dispersion coefficients were processed from the unit cell scale solutions for velocity and temperature fields. The unit cell scale governing equations were solved by assuming laminar and steady fluid flow with constant thermophysical properties. In this section, unit cell scale computation of the unsteady flow is carried out in order to determine the effect of the unsteadiness on porous media transport properties. The flow field within a unit cell is modeled with FLUENT assuming an unsteady two-dimensional flow. The 1st-order implicit formulation is utilized for the temporal discretization of the transient term and the power-law scheme is applied in the spatial discretization. The pressure–velocity coupling is handled with the SIMPLC algorithm. Under-relaxation factors are applied in the solution of momentum and continuity equations in order to enhance the stability of the Gauss–Seidel iterative solver. The working fluid chosen for this study is air with constant physical properties. A grid independent study is conducted by using a progression of grid sizes. Testing with 1600, 6400, 14,1400, and 90,000 nodes showed that the 6400 nodes is adequate.

The solution is started by initializing the field variables and specifying the mass flow rate and the mean flow angle. The flow is assumed to be aligned with the stream-wise principal axis X , which makes an angle of 45° with the unit cell coordinate x , as shown in Fig. 1. The mass flow rate is varied in order to cover the range of Reynolds numbers, Re_{luc} , between 1 and 2000. The transient solver is applied by specifying a fixed time step of 10^{-5} s while running, at-most, 40 iterations per time step. The unsteady solutions, which are characterized by vortex shedding, occur after nearly 15,000 iterations (an average of all the cases). Once a time-periodic solution is established, the transient calculation is continued for at least another 1000 time steps and the ensemble averaging is initiated.

4.1. Results

Here, the results of unsteady flow are presented in terms of the ensemble averages of quantities of interest. Mainly, the dimensionless pressure gradient $-\frac{\nabla(p)^f l_{uc}}{\mu_f \langle \tilde{u} \rangle}$ versus Re_{luc} is shown (Fig. 23) for steady flow and unsteady simulations. The figure shows that the dimensionless pressure gradients stay nearly constant for Re_{luc} less than 10, then increase significantly as the inertial effects dominate. Furthermore, the unsteady solution bifurcates from the steady solution when Re_{luc} is around 10^2 . The steady solution results are within 10% of the unsteady results.

Dispersion in porous media is comprised of two mechanism, molecular diffusion and thermal dispersion. These are represented by the RHS in the above equation as the first and the second term, respectively. In the first term, the stagnant conductivity k_{st} depends on the thermophysical properties of fluid and solid phases' and the porous medium structural geometry. Whereas, the second term accounts for thermal dispersion or enhanced heat transfer which occurs in response to the interaction between the local spatial fluctuations of velocity and temperature at the pore scale.

$$(\rho c_p)_f \langle \tilde{u} \rangle \cdot \nabla \langle T \rangle = \nabla \cdot \{ k_{st} \nabla \langle T \rangle + \rho_f c_{pf} \langle \tilde{u} \tilde{T} \rangle \} \quad (47)$$

Usually the latter dispersion heat flux term is modeled as the gradient of the spatial averaged temperature with the coefficient being the dispersion thermal conductivity [50]. Recently, Nakayama et al. [51] showed that the gradient diffusion hypothesis that has been often adopted [52] for modeling the thermal dispersion heat flux can be derived from a transport equation for thermal dispersion heat flux based on the Navier–Stokes and energy equations.

Therefore, thermal dispersion can be modeled as

$$-\rho_f c_{pf} \langle \tilde{u} \tilde{T} \rangle = \mathbf{k}_{dis} \cdot \nabla \langle T \rangle \quad (48)$$

where \mathbf{k}_{dis} is defined as the flow-driven thermal dispersion conductivity. The flow-driven dispersion diffusivity of the stream-wise transport is defined as

$$\epsilon_{H_{xx}} = \frac{k_{xx}}{\rho_f c_{pf}} \equiv -\frac{\langle \tilde{u} \tilde{T} \rangle}{\partial \langle T \rangle / \partial X} \quad (49)$$

Earlier we showed that the volume averaging process of the momentum equation resulted in an expression which accounts for hydrodynamic dispersion and is given as $\rho_f c_{pf} \langle \tilde{u} \tilde{v} \rangle$.

Hence the hydrodynamic dispersion diffusivity can be defined as follows:

$$\epsilon_{M_{xx}} = -\frac{\langle \tilde{u} \tilde{v} \rangle}{\partial \langle u \rangle / \partial X} \quad (50)$$

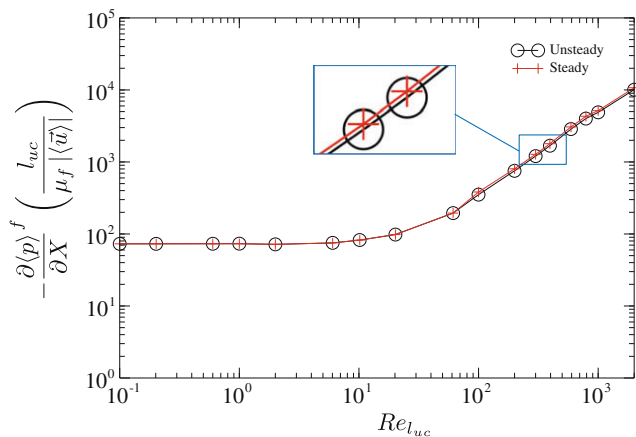


Fig. 23. Dimensionless plot of the pressure gradient.

where $\epsilon_{M_{xx}}$ is the coefficient of the momentum dispersion transport in the stream-wise direction.

Implementation of the thermal dispersion formulation with FLUENT is cumbersome. Thus, for the purposes of this study, which was the determination of unsteadiness on the dispersion coefficients, we used the flowfield solutions and, in conjunction with Reynolds analogy between momentum and energy transfer, compute the hydrodynamic dispersion and by analog assign it to be the thermal dispersion as well. Following Niu and Simon [53] we apply the analogy between the thermal and momentum dispersion as $\epsilon_{H_{xx}} = \epsilon_{M_{xx}}$.

Animated sequences of streamlines and hydrodynamic dispersion are prepared for the unsteady flow case. Figs. 24 and 25 show the stream-function and dispersion values sampled at various times within a full-cycle (see Fig. 26).

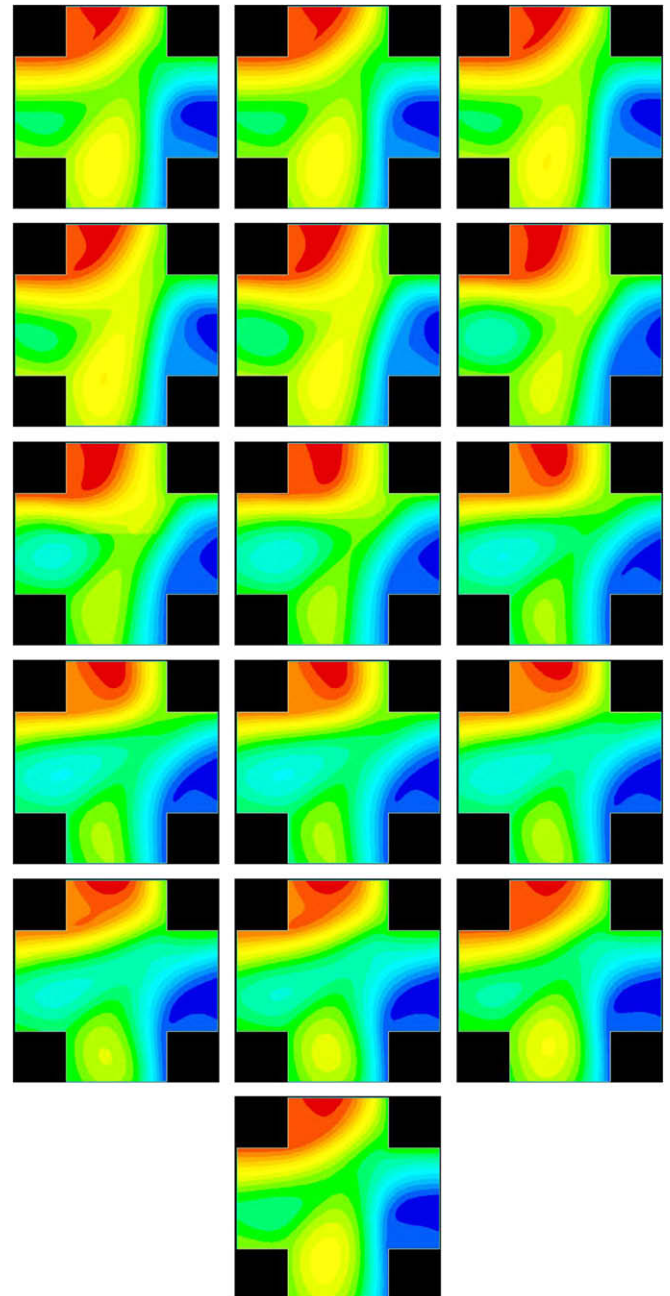


Fig. 24. Stream-function, $\alpha = 45^\circ$ and $Re_{luc} = 790$, full cycle τ at various non-dimensional time points ranging from $t/\tau = 0$ to $t/\tau = 1$.

Fig. 24 show a sequence of streamlines for a case where the mean flow angle, α , 45° and $Re_{luc} = 790$ for a full cycle of period, τ , starting at a dimensionless time $t/\tau = 0$. We can see that the a counter clock-wise vortex is developed behind the upstream square cylinder in southwest corner of the unit cell; and another clock-wise vortex is developing on top of the same cylinder. The clock-wise vortex grows in time. Fig. 27 shows the instantaneous flow angle changes.

Figs. 28 and 29 show a comparison between steady state and unsteady ensemble averaged hydrodynamic dispersion. It is apparent that dispersion of both cases are in general agreement. The REV space-averaged dispersion values from the steady and unsteady flow calculations are within 3%.

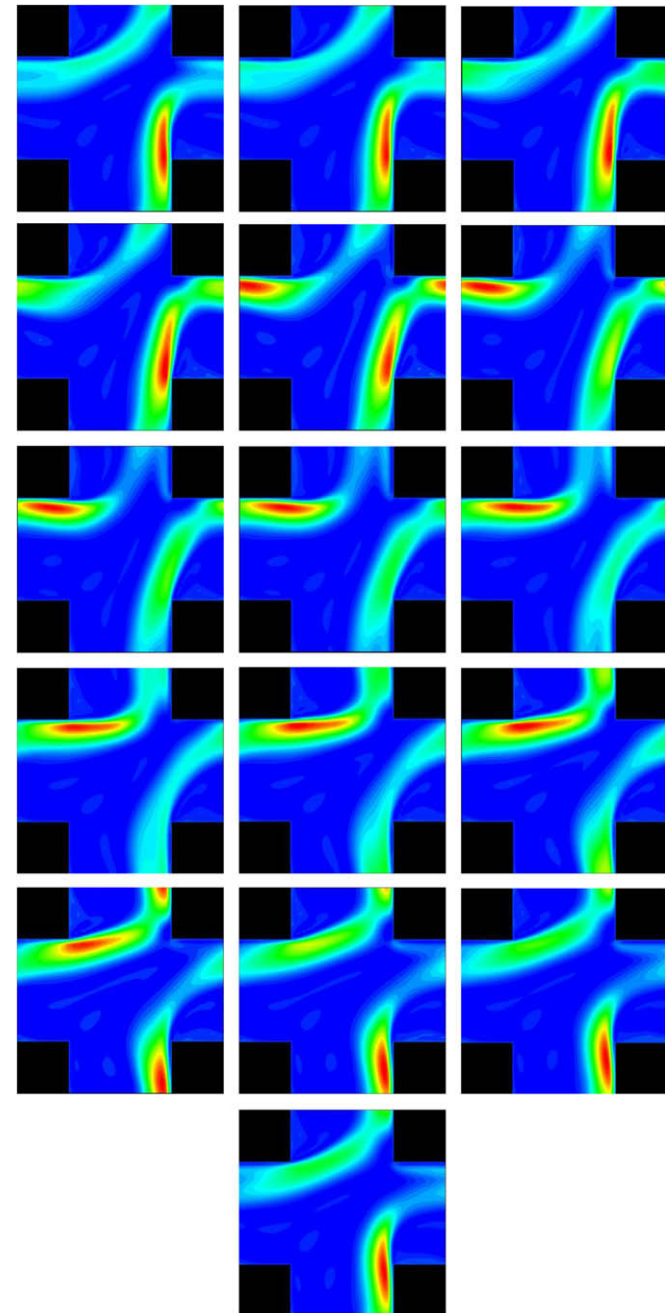


Fig. 25. Hydrodynamic dispersion, $\alpha = 45^\circ$ and $Re_{luc} = 790$, full cycle τ at various non-dimensional time points ranging from $t/\tau = 0$ to $t/\tau = 1$.

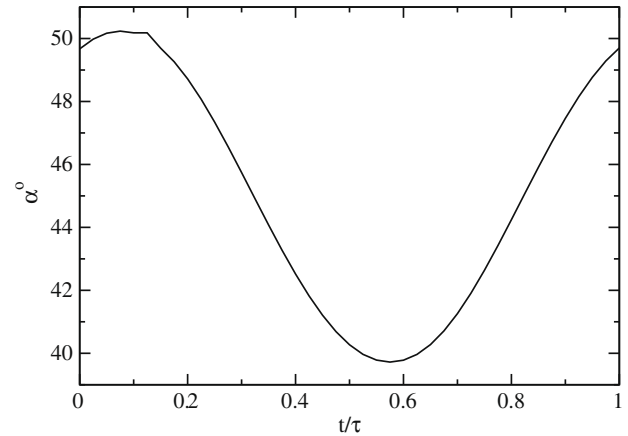


Fig. 26. Flow angle vs dimensionless time.

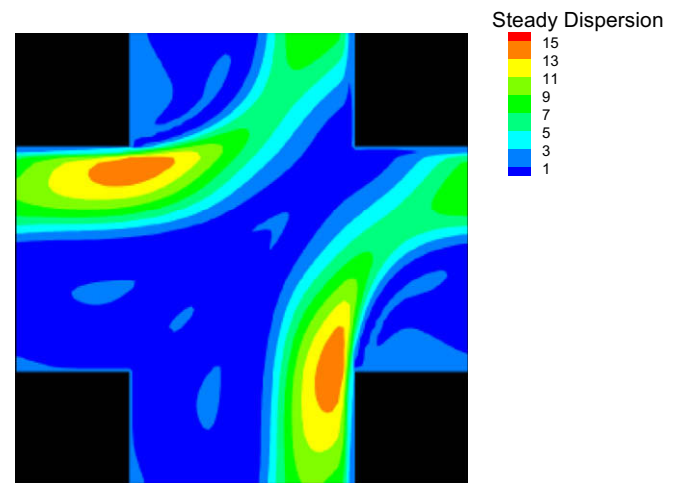


Fig. 27. Instantaneous flow angle for full cycle.

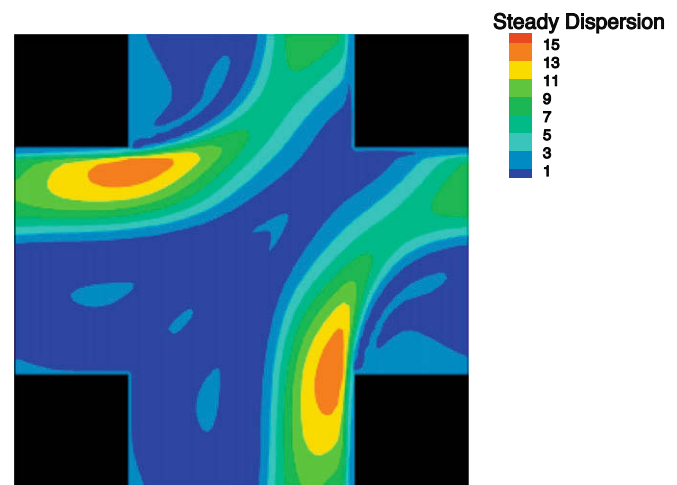


Fig. 28. Hydrodynamic dispersion, $\alpha = 45^\circ$ and $Re_{luc} = 790$, steady flow.

5. Summary and conclusions

A data base is constructed for *elementary representative volume* (REV) unit cell consisting of a fluid phase and heat generating solid phase by analyzing it with an imposing flow having various angles

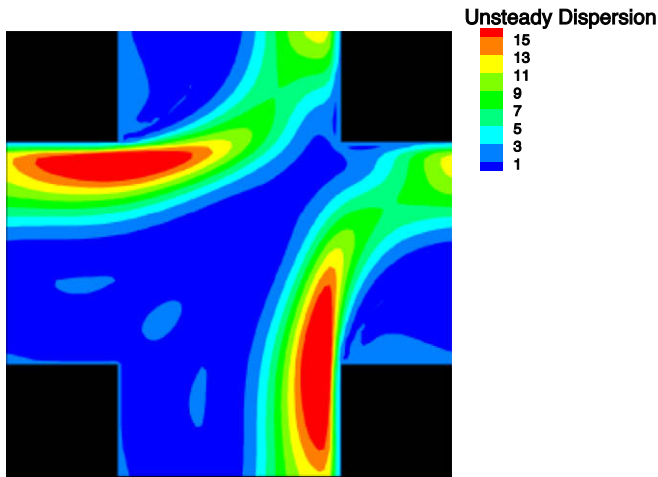


Fig. 29. Ensemble-averaged hydrodynamic dispersion for a full cycle τ , $\alpha = 45^\circ$ and $Re_{uc} = 790$, unsteady flow.

of approach relative to the unit cell and a range of Reynolds number. The velocity and temperature fields within the REV are processed in order to characterize the porous medium in terms of its effective properties.

Using a computational unit cell model, the flow resistances are cast in terms of the porous medium permeability, which accounts for viscous drag, and the inertial coefficient, which accounts for form drag. We found that the permeability of the isotropic medium is uniform and independent of the flow angle, while for the anisotropic medium, the permeability varies nearly linearly between the two principal permeabilities (along the porous medium principal axes or axes of porous medium structural symmetry). We also found that the permeability decreases with increased solid volume fraction or increased porosity. Furthermore, we determined the principal apparent permeabilities which lumps the effects of both the “material permeability and inertial coefficient effects. It was shown that the apparent permeability attains a maximum value along the principal axes and diminishes with either increasing approaching flow angle or increasing Reynolds number. The interfacial heat transfer coefficients are dependent on both the unit cell Reynolds number and the mean flow angle. The heat transfer coefficients are of minimal values when the flow is issued along the principal axes, since such flow is similar to a fully developed duct flow with zones of recirculating flow in the intra-space between the solids; and they increase substantially for the cases oblique flow. Likewise, the dispersion values are dependent on both the unit cell Péclet number and the mean flow angle. However, the flow driven stream-wise dispersion values is much larger the cross-stream dispersion values.

The unsteady unit cell computations show that the dimensionless pressure gradient curve bifurcates from the steady state calculated curve when the unit cell Reynolds number is nearly 10^2 , which is indicative of the onset of flow unsteadiness and is characterized by the alternating vortex shedding in the vicinity of the leeward face of the solids in the southwest corner of the unit cell. The hydrodynamic dispersion is used with Reynolds analogy between momentum and energy transfer to estimate thermal dispersion, as processed from the velocity field computations. We found that the REV averaged dispersion value of the steady flow dispersion and likewise REV averaged and ensemble average dispersion value of unsteady flow calculations are within 17%. Whereas the pressure gradient steady and unsteady calculations are within 10%.

Acknowledgements

The authors would like to acknowledge the support of The University of Minnesota Supercomputing Institute for Advanced Computational Research for providing the computational resources.

References

- [1] M. Shapiro, H. Brenner, Dispersion/reaction model of aerosol filtration by porous filters, *J. Aerosol Sci.* 21 (1) (1990) 97–125.
- [2] F.E. Curry, C.C. Michel, A fiber matrix model of capillary permeability, *Microvascular Res.* 20 (1980) 96–99.
- [3] R.E. Larson, J.L. Higdon, Microscopic flow near the surface of two-dimensional porous media. Part 2. Transverse flow, *J. Fluid Mech.* 178 (1987) 119–136.
- [4] O. Coulaud, P. Morel, J.P. Caltagirone, Numerical modelling of nonlinear effects in laminar flow through a porous medium, *J. Fluid Mech.* 190 (1988) 393–407.
- [5] D.A. Edwards, S.P. Bar-Yoseph, E.M. Bar-Yoseph, The influence of Reynolds number upon the apparent permeability of spatially periodic arrays of cylinders, *Phys. Fluids A* 2 (1) (1990) 45–55.
- [6] C.K. Ghaddar, On the permeability of unidirectional fibrous media: a parallel computational approach, *Phys. Fluids* 7 (11) (1995) 2563–2586.
- [7] D. Nagelhout, M.S. Bhat, J.C. Heinrich, D.R. Poirier, Permeability for flow normal to a sparse array of fibers, *Mater. Sci. Eng. A – Struct. Mater. Properties Microstruct. Process.* 191 (1–2) (1995) 203–208.
- [8] A.R. Martin, C. Saltiel, W. Shyy, Frictional losses and convective heat transfer in sparse, periodic cylinder arrays in cross flow, *Int. J. Heat Mass Transfer* 41 (15) (1998) 2383–2397.
- [9] S.L. Lee, J.H. Yang, Modeling of Darcy–Forchheimer drag for fluid flow across a bank of circular cylinders, *Int. J. Heat Mass Transfer* 40 (13) (1997) 3149–3155.
- [10] D.L. Koch, A.J.C. Ladd, Moderate Reynolds number flows through periodic and random arrays of aligned cylinders, *J. Fluid Mech.* 349 (1997) 31–66.
- [11] T.D. Papathanasiou, B. Markicevic, E.D. Dendy, A computational evaluation of the Ergun and Forchheimer equations for fibrous porous media, *Phys. Fluids* 13 (10) (2001) 2795–2804.
- [12] V.B. Grannis, Sparrow, Numerical simulation of fluid flow through an array of diamond-shaped pin fins, *Numer. Heat Transfer, Part A* 19 (1991) 381–403.
- [13] S. Ergun, Fluid flow through packed columns, *Chem. Eng. Prog. S* 48 (1952) 89.
- [14] H. Brenner, Dispersion resulting from flow through spatially periodic porous media, *Philos. Trans. Roy. Soc. (London)* 297 (1980) 81–133.
- [15] R.G. Carbonell, S. Whitaker, Dispersion in pulsed system-II: Theoretical developments for passive dispersion in porous media, *Chem. Eng. Sci.* 38 (1983) 1795–1802.
- [16] A. Eidsath, R.G. Carbonell, S. Whitaker, Dispersion in pulsed systems – III. Comparison between theory and experiment for packed beds, *Chem. Eng. Sci.* 38 (1983) 1803–1816.
- [17] D.J. Gunn, C. Pryce, Dispersion in packed beds, *Trans. Inst. Chem. Eng.* 47 (1969) 341–350.
- [18] D.L. Koch, R.G. Cox, H. Brenner, J.F. Brady, The effect of order on dispersion in porous media, *J. Fluid Mech.* 200 (1989) 178–188.
- [19] D.A. Edwards, M. Shapiro, H. Brenner, M. Shapira, Dispersion of inert solutes in spatially periodic, two-dimensional model porous media, *Transp. Porous Media* 6 (4) (1991) 337–358.
- [20] M. Sahaoui, M. Kaviany, Slip and no-slip temperature boundary conditions at interface of porous, plain media: convection, part 1 – formulation, 28th National Heat Transfer Conference and Exhibition, August 9–12 1992, vol. 193, American Society of Mechanical Engineers, Heat Transfer Division, (Publication) HTD, San Diego, CA, USA, 1992, pp. 25–33.
- [21] M. Sahaoui, M. Kaviany, Slip and no-slip temperature boundary conditions at interface of porous, plain media: convection, part 2 – results, 28th National Heat Transfer Conference and Exhibition, August 9–12, vol. 193, American Society of Mechanical Engineers, Heat Transfer Division, (Publication) HTD, San Diego, CA, USA, 1992, pp. 35–47.
- [22] M. Sahaoui, M. Kaviany, Slip and no-slip boundary conditions at interface of porous, plain media, *Int. J. Heat Mass Transfer* 35 (1992) 927–943.
- [23] E. Arquis, J.P. Caltagirone, P. Le Breton, Determination des propriétés de dispersion d’un milieu périodique a partir de l’analyse locale des transferts, *C.R. Acad. Sci. Paris II* (313) (1991) 1087–1092.
- [24] E. Arquis, J.P. Caltagirone, A. Delmas, Derivation in thermal conductivity of porous media due to high interstitial flow velocity, in: *Proc. 22nd Int. Thermal Conductivity Conf.*, Tempe, AZ, 1993.
- [25] F. Kuwahara, A. Nakayama, H. Koyama, A numerical study of thermal dispersion in porous media, *J. Heat Transfer – Trans. ASME* 118 (3) (1996) 756–761.
- [26] F. Kuwahara, A. Nakayama, Numerical determination of thermal dispersion coefficients using a periodic porous structure, *J. Heat Transfer – Trans. ASME* 121 (1) (1999) 160–163.
- [27] H.P.A. Souto, C. Moyne, Dispersion in two-dimensional periodic porous media. 2. Dispersion tensor, *Phys. Fluids* 9 (8) (1997) 2253–2263.
- [28] S. Didierjean, H.P.A. Souto, R. Delannay, C. Moyne, Dispersion in periodic porous media. Experience versus theory for two-dimensional systems, *Chem. Eng. Sci.* 52 (12) (1997) 1861–1874.

- [29] N. Wakao, S. Kagueli, T. Funazkri, Effect of fluid dispersion coefficients on particle-to-fluid heat transfer coefficients in packed beds, *Chem. Eng. Sci.* 34 (1979) 325–336.
- [30] W.E. Ranz, W.R. Marshall, Evaporation from drops I, *Chem. Eng. Prog.* 48 (3) (1952) 141–146.
- [31] W.E. Ranz, W.R. Marshall, Evaporation from drops II, *Chem. Eng. Prog.* 48 (4) (1952) 173–180.
- [32] N. Wakao, S. Kagueli, *Heat and Mass Transfer in Packed Beds*, Gordon and Breach, New York, 1982.
- [33] A.R.H. Cornish, Note on minimum possible rate of heat transfer from a sphere when other spheres are adjacent to it, *Trans. Inst. Chem. Eng.* 43 (1965) 332–333.
- [34] W.M. Kays, A.L. London, *Compact Heat Exchangers*, second ed., McGraw-Hill, New York, 1964.
- [35] A. Zukauskas, Heat transfer from tubes in cross flow, *Adv. Heat Transfer* 18 (1987) 87–159.
- [36] K.K. Kar, A. Dybbs, Internal heat transfer coefficients of porous metals, in: J.V. Beck, L.S. Yao (Eds.), *Heat Transfer in Porous Media*, vol. 22, ASME HTD, 1982, pp. 81–91.
- [37] A. Dybbs, J.X. Ling, Heat transfer in porous media: experiments and physical model, in: H.R. Jacobs (Ed.), *ASME Proceedings of the 1988 National Heat Transfer Conference*, vol. 1, 1988.
- [38] F. Kuwahara, M. Shirota, A. Nakayama, A numerical study of interfacial convective heat transfer coefficient in two-energy equation model for convection in porous media, *Int. J. Heat Mass Transfer* 44 (6) (2001) 1153–1159.
- [39] A. Nakayama, F. Kuwahara, T. Hayashi, Numerical modelling for three-dimensional heat and fluid flow through a bank of cylinders in yaw, *Journal of Fluid Mechanics* 498 (2004) 139–159.
- [40] A. Nakayama, F. Kuwahara, T. Umemoto, T. Hayashi, Heat and fluid flow within an anisotropic porous medium, *J. Heat Transfer – Trans. ASME* 124 (4) (2002) 746–753.
- [41] R. Viskanta, Modeling of transport phenomena in porous media using a two-energy equation model, in: *ASME/JSM Thermal Engineering Conference*, vol. 3, 1995.
- [42] S.V. Patankar, C.H. Liu, E.M. Sparrow, Fully developed flow and heat transfer in ducts having streamwise-periodic variations of cross-sectional area, *J. Heat Transfer – Trans. ASME* 99 (1977) 180–186.
- [43] S.V. Patankar, *Numerical Heat and Fluid Flow*, Hemisphere Publishing Corporation, Washington, DC, 1980.
- [44] P.S. Sathyamurthy, K.C. Karki, Internal Report, Innovative Research, Inc., 1992.
- [45] K.M. Kelkar, S.V. Patankar, Numerical prediction of flow and heat transfer in a channel with heated blocks, *Comput Aided Des Electron Packaging – ASME-EEP* (1992) 25–33.
- [46] S.V. Patankar, A calculation procedure for two-dimensional elliptic situations, *Numer. Heat Transfer* 5 (1981) 409–425.
- [47] F.A.L. Dullien, *Porous Media: Fluid Flow and Pore Structure*, Academic press, San Diego, 1992.
- [48] M. Sahraoui, M. Kaviany, Slip no-slip temperature boundary conditions at the interface of porous plain media: convection, *Int. J. Heat Mass Transfer* 37 (6) (1994) 1029–1044.
- [49] Mebrouk Saada, Chikh Salah, Antonio Campo, *Heat and Mass Transfer* 42 (2006) 995–1006.
- [50] D.L. Koch, J.F. Brady, Dispersion in fixed beds, *J. Fluid Mech.* 154 (1985) 399–427.
- [51] A. Nakayama, F. Kuwahara, Y. Kodama, An equation for thermal dispersion flux transport and its mathematical modeling for heat and fluid flow in porous medium, *J. Fluid Mech.* 563 (2006) 81–96.
- [52] A. Amiri, K. Vafai, Analysis of dispersion effects and non-thermal equilibrium: non-Darcian, variable porosity incompressible flow through porous media, *Int. J. Heat Mass Transfer* 37 (6) (1994) 939–954.
- [53] Y. Niu, T.W. Simon, Direct measurement of eddy transport and thermal dispersion in high-porosity matrix, *J. Thermophys. Heat Transfer* 20 (2006) 101–106.